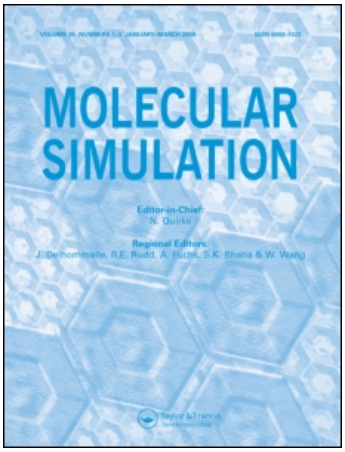

Molecular Simulation
Publication details, including instructions for authors and subscription information:
http://www.informaworld.com/smpp/title~content=t713644482

Temperature-and-density-scaling Monte Carlo: methodology and the canonical thermodynamics of Lennard-Jonesium

John P. Valleau[a]
[a] Chemical Physics Theory Group, Department of Chemistry, University of Toronto, Toronto, Ont., Canada

To cite this Article Valleau, John P.(2005) 'Temperature-and-density-scaling Monte Carlo: methodology and the canonical thermodynamics of Lennard-Jonesium', Molecular Simulation, 31: 4, 223 — 253
To link to this Article: DOI: 10.1080/08927020500035937
URL: http://dx.doi.org/10.1080/08927020500035937

Molecular Simulation, Vol. 31, No. 4, 15 April 2005, 223–253

Taylor & Francis
Taylor & Francis Group

Temperature-and-density-scaling Monte Carlo: methodology and the canonical thermodynamics of Lennard-Jonesium

JOHN P. VALLEAU*

Chemical Physics Theory Group, Department of Chemistry, University of Toronto, Toronto, Ont., Canada M5S 3H6

(Received September 2004; in final form September 2004)

Umbrella sampling was used to study, within a Monte-Carlo run, substantial ranges of both temperature and density: i.e. "temperature-and-density-scaling Monte-Carlo" (TDSMC). The paper reviews in detail some of the theory and the practicalities of using the TDSMC technique. For example, we discuss how to generate an appropriate sampling distribution, and the question of appropriate error analysis for TDSMC data. In order to test whether the sampling efficiency might be improved by "stratifying", the entire investigation was carried out in two ways: by covering the target region of thermodynamic space in a single TDSMC run, and by independently segmenting the same target region into three overlapping subregions, investigated by separate TDSMC runs: the results and relative efficiencies are compared.

These matters, and the potential of the method, are illustrated by application to a Lennard-Jones fluid. The target region covered a substantial region of the thermodynamic space, including the upper part of the gas–liquid coexistence curve, and the TDSMC run provides direct and accurate estimates of relative free energy throughout the region, along with other properties such as the pressure, internal energy, chemical potential and heat capacity. The results are also used to characterise the thermodynamics of the liquid–gas transition in the canonical ensemble. The precision of all these results is substantially better than in other simulation methods of studying such properties.

Keywords: Monte-Carlo; Thermodynamic scaling; Equation of state; Canonical ensemble; Coexistence; Lennard-Jones

1. Introduction

The purpose of "thermodynamic scaling" Monte Carlo is to study a substantial *range* of thermodynamic states simultaneously, within a single Monte Carlo run. This is a particular example of "umbrella sampling" [1]. It requires that the Monte Carlo Markov chain sample on a distribution $\pi(\mathbf{X})$ which includes adequately the system configurations $\mathbf{X}$ important to *all* the thermodynamic states in the target range. If this can be accomplished, it leads immediately to information that would not be directly accessible from (even very many) runs at individual states throughout the range. In particular, it gives a direct determination of relative *free energies* between every pair of states in the targetted region. This makes the technique especially useful in the study of phase transitions, where accurate free energy profiles are often crucial and difficult to obtain. The other challenge in the computational exploration of phase changes is often the problem of extremely slow sampling (known as "quasi-ergodicity") characteristically experienced in conventional simulations near phase transitions; happily the thermodynamic scaling approach goes far to eliminating this problem as well.

"Thermodynamic scaling" can come in a variety of flavours. Most reported results involve a one-dimensional range of thermodynamic states. For example, it is easy to cover a large range of temperature in a single run: "temperature-scaling" Monte Carlo (TSMC) [2–4]. Alternatively, for fluids for example, one could sample over a range of density ρ at fixed temperature [5,6]: "density-scaling" (DSMC); this range could for example embrace the density gap of the liquid–gas coexistence in a fluid [7]. Similar techniques could be applied to the order parameter for transitions in other systems, such as the magnetisation in Ising-like models [8,9]. It is also possible to examine a range of system *models*, as defined by their Hamiltonians—"Hamiltonian-scaling"; this was done in the original paper [1], and there have been many other interesting applications, e.g. [10–6]. Such one-dimensional investigations can be very useful. However, *two* thermodynamic variables are required to specify the behaviour of even a one-component fluid system, and we will see that it

*Corresponding author. E-mail: jvalleau@chem.utoronto.ca

Molecular Simulation
ISSN 0892-7022 print/ISSN 1029-0435 online © 2005 Taylor & Francis Group Ltd
http://www.tandf.co.uk/journals
DOI: 10.1080/08927020500035937

is much more powerful and efficient to "scale" with respect to the two thermodynamic variables simultaneously, thus covering a finite—even a substantial—part of the thermodynamic space in each run. In the present example, we study a fluid throughout ranges of both temperature and density: "temperature-and-density-scaling" Monte-Carlo, or TDSMC.

This paper reports an extensive study along these lines, where TDSMC is applied to a familiar test system: the Lennard-Jones fluid. We report in this paper free energies in the canonical ensemble, and also the internal energy, pressure, compressibility, heat capacity and internal pressure; from these we can derive other canonical thermodynamic functions. The overall target region encompasses the critical region and part of the liquid–gas coexistence curve, and we go on to explore this behaviour. A cursory review of the relevance of the TDSMC method to the study of phase transitions appeared previously [17], and an application to square-well fluids was briefly reported [18]. However, there has previously been no detailed examination of the practical details of carrying out such investigations; this paper goes beyond that, to evaluate various alternative strategies for carrying out and applying TDSMC. There has also been no previous systematic presentation of the Lennard-Jones thermodynamic and coexistence data in the canonical ensemble reported here, which appear to be substantially more precise than earlier results.

The most basic results in a TDSMC investigation are the relative free energies throughout the target (T,ρ) region (Section 3). One also obtains the other thermodynamic properties mentioned above, but it is interesting that there is more than one way of doing so: we obtain each of them by two different routes, and compare the efficiency of the two approaches (Section 4). The free energy contours allow location of the gas–liquid coexistence (again in various ways), and the rest of the thermodynamics of the transition then follows (Section 5).

We report in this paper the Helmholtz free energy and other thermodynamic functions, at states defined by (T,ρ), for a fixed number of particles N — that is, results appropriate to the canonical ensemble. Of course, knowledge of free energy as a function of these variables provides in principle *complete* thermodynamic information, at least in the thermodynamic limit. In that limit the behaviour, as described by the equations of state, is the same whatever ensemble might be used to generate it. However, practical simulations necessarily deal with *finite* systems—even rather small ones. In that case differing properties are allowed to fluctuate in the various ensembles, and as a result the behaviours as derived in them will no longer coincide; these discrepancies will be particularly noticeable in the region of phase transition. It would be of interest to *compare* the behaviours in different ensembles for the small systems to which we are restricted in simulation. It turns out that this can be done very conveniently using the results of a TDSMC study: in a following paper [19], we examine in detail the thermodynamics of the Lennard-Jones fluid in the *isothermal–isobaric* ensemble, by an alternative analysis of the very data generated in the TDSMC study reported here. Elsewhere, we have described the use of similar data to generate results for the so-called "Gibbs ensemble" [20], and expect shortly to describe their application to the grand canonical ensemble [21].

A matter of interest is the analysis of simulation results in order to examine the critical behaviour of model systems. Except for a few remarks, we postpone such an analysis of the present canonical results for Lennard-Jonesium. One reason is that the methods required for such anlysis are still under development. At the same time, it is likely that canonical results will remain less useful in this regard than those of other ensembles, due to severely constrained density fluctuations; this constitutes a further motive for the application of TDSMC data to other ensembles.

The following section concerns the theory and application of the TDSMC method to a simple fluid system.

2. The TDSMC method

2.1 General description

In TDSMC, we calculate the complete thermodynamics of a fluid throughout some target region involving ranges of both temperature T and density ρ. It is convenient to discuss this by focussing first on the estimation of the relative canonical Helmholtz free energy throughout that region.

Suppose a model system of N particles, described in the space of its configurations $\mathbf{q}^N \equiv (\mathbf{q}_1, \mathbf{q}_2, \ldots \mathbf{q}_N)$ and characterized by a potential energy function $U(\mathbf{q}^N)$. For now we consider structureless particles, so $\mathbf{q}$ is simply a position vector (but the results are easily generalized). Consider any two thermodynamic states in the target region, specified by their temperatures and densities, (T_i,ρ_i) and (T_j,ρ_j). The difference of their reduced canonical Helmholtz free energies may be written

$$\frac{A_j^{\mathrm{Can}}}{k_{\mathrm{B}}T_j} - \frac{A_i^{\mathrm{Can}}}{k_{\mathrm{B}}T_i} = \frac{3}{2}\log\left(\frac{T_i}{T_j}\right) + \log\left(\frac{Z_i}{Z_j}\right), \qquad (1)$$

where $A_i^{\mathrm{Can}} \equiv A^{\mathrm{Can}}(N, T_i, \rho_i)$ is the canonical free energy, k_{B} is Boltzmann's constant and $Z_i = Z(N, T_i, \rho_i)$ is a "configuration integral". (The notation, here and elsewhere, specifies the ensemble explicitly, anticipating the comparison of results in various ensembles [19–21]). Explicitly, the ratio Z_i/Z_j of configuration integrals in equation (1) is given by

$$\frac{Z_i}{Z_j} \equiv \frac{\int_{V_i} \mathrm{d}\mathbf{q}^N \exp(-\beta_i U(\mathbf{q}^N))}{\int_{V_j} \mathrm{d}\mathbf{q}^N \exp(-\beta_j U(\mathbf{q}^N))} \qquad (2)$$

where $\rho_i \equiv N/V_i$ and $\beta_i \equiv (k_{\mathrm{B}}T_i)^{-1}$; as indicated, the integrals extend over hypervolumes V_i^N and V_j^N appropriate to the two densities ρ_i and ρ_j (for N particles). It is important that the desired quantity is a *ratio* of integrals, because this

is the only kind of quantity whose estimation is possible using Markov-chain Monte Carlo sampling [See e.g. 22].

However, as it stands, equation (2) is not convenient (except when $\rho_i = \rho_j$) because of the differing hypervolumes of the two configuration spaces. This difficulty is trivially overcome, however, by describing the configurations in terms of "reduced" coordinates $\mathbf{r}$, such that in Z_i, for example,

$$\mathbf{r} \equiv \frac{\mathbf{q}}{L_i}, \quad \text{with } L_i \equiv V_i^{1/3}, \tag{3}$$

now the configurations at *every* density ρ can be described by $\mathbf{r}^N$, in the reduced configuration space (of unit hypervolume). Indeed, to *each* configuration $\mathbf{r}^N$ corresponds a configuration $\mathbf{q}^N$ at *every* density $\rho_i = N/L_i^3$, and the corresponding potential energy at any particular ρ_i may be written as a function $U(\mathbf{r}^N,L_i)$. (The explicit form of this function for the Lennard-Jones fluid is given below at equation (12); an analogous form exists for any configurational property.) Then equation (2) becomes

$$\frac{Z_i}{Z_j} = \frac{V_i^N \int_1 \mathrm{d}\mathbf{r}^N \exp(-\beta_i U(\mathbf{r}^N, L_i))}{V_j^N \int_1 \mathrm{d}\mathbf{r}^N \exp(-\beta_j U(\mathbf{r}^N, L_j))} \equiv \frac{V_i^N Z_i^{\mathrm{ex}}}{V_j^N Z_j^{\mathrm{ex}}}, \tag{4}$$

where we define "excess" configurational integrals like Z_i^{ex}, each of which extends over a reduced configuration space of unit volume. Recalling that the "ideal" free energy A^{id} is given by

$$\beta A^{\mathrm{id}}/N = \text{const} - \left(\frac{3}{2}\right)\log(T) + \log(\rho), \tag{5}$$

we see that the ratio $Z_i^{\mathrm{ex}}/Z_j^{\mathrm{ex}}$ gives the differences of the reduced canonical *excess* free energy, $\beta(A^{\mathrm{ex}})^{\mathrm{Can}} \equiv \beta A^{\mathrm{Can}} - \beta A^{\mathrm{id}}$, according to

$$\Delta_{ij}(\beta A^{\mathrm{ex}})^{\mathrm{Can}} \equiv \beta_j \left(A_j^{\mathrm{ex}}\right)^{\mathrm{Can}} - \beta_i \left(A_i^{\mathrm{ex}}\right)^{\mathrm{Can}}$$

$$= \log\left(\frac{Z_i^{\mathrm{ex}}}{Z_j^{\mathrm{ex}}}\right). \tag{6}$$

It is convenient in TDSMC, therefore, to estimate directly $Z_i^{\mathrm{ex}}/Z_j^{\mathrm{ex}}$ and thus to derive the relative reduced canonical excess free energy, using equation (6).

This estimate is to be made by carrying out a Markov-chain Monte Carlo sampling in the reduced configuration space $\mathbf{r}^N$, with a limiting distribution $\pi(\mathbf{r}^N)$. Using mathematical identities we can transform the identity in equation (4):

$$\frac{Z_i^{\mathrm{ex}}}{Z_j^{\mathrm{ex}}} \equiv \frac{\int_1 \mathrm{d}\mathbf{r}^N \pi(\mathbf{r}^N)[\exp(-\beta_i U(\mathbf{r}^N, L_i)/\pi(\mathbf{r}^N)]}{\int_1 \mathrm{d}\mathbf{r}^N \pi(\mathbf{r}^N)[\exp(-\beta_j U(\mathbf{r}^N, L_j)/\pi(\mathbf{r}^N)]}$$

$$\times \frac{\int_1 \mathrm{d}\mathbf{r}^N \pi(\mathbf{r}^N)}{\int_1 \mathrm{d}\mathbf{r}^N \pi(\mathbf{r}^N)}$$

$$\equiv \frac{\langle \exp(-\beta_i U(\mathbf{r}^N, L_i))/\pi(\mathbf{r}^N)\rangle^{\pi}}{\langle \exp(-\beta_j U(\mathbf{r}^N, L_j))/\pi(\mathbf{r}^N)\rangle^{\pi}}, \tag{7}$$

where the superscript π indicates the distribution over which the average is taken. We see that the desired ratio is merely that of two straightforward averages based on the sampling distribution $\pi(\mathbf{r}^N)$. Such averages can simply be collected during the run in the usual way, and *for as many states* (T,ρ) *as one wishes* (within the target region sampled by $\pi(\mathbf{r}^N)$), and will then allow estimation of the relative free energy between every pair of these states. This ratio of averages (7) is, of course, asymptotically unbiassed.

(In principle one could instead store as histograms the data required in order to re-create the ratio (7) by "reweighting". Two-dimensional information is, of course, required, e.g. energy histograms for every density of interest, so a very large array of storage elements would be required. Deciding in advance the energy and density intervals necessary to reduce adequately the biasses inherent in the use of histograms could be difficult, especially if one hoped to apply the TDSMC results to other ensembles in which the density fluctuates (cf. the following paper). We find this less attractive than simply collecting during the run the (unbiassed) data for a dense regular grid of thermodynamic states; accurate interpolation to give continuous results, if desired, is then easy, as described in the Section below.)

This is all simple, and formally correct for any sampling distribution $\pi(\mathbf{r}^N)$. However, one must in practice be able to *find* a distribution which will give good estimates of the required averages throughout a substantial (T,ρ) region. We postpone consideration of this requirement for discussion in the following subsection.

Along with relative free energy, one would like to estimate quantities which can be expressed as canonical averages at each state (T_i,ρ_i). The canonical average $\langle R(\mathbf{q}^N)\rangle^{\mathrm{Can}}$ of any configurational function $R(\mathbf{q}^N) \equiv R(\mathbf{r}^N, L_i)$ can be written, again employing identities, as

$$\langle R(\mathbf{q}^N)\rangle^{\mathrm{Can}}$$

$$\equiv \frac{\int_{V_i} \mathrm{d}\mathbf{q}^N R(\mathbf{q}^N) \exp(-\beta_i U(\mathbf{q}^N))}{\int_{V_i} \mathrm{d}\mathbf{q}^N \exp(-\beta_i U(\mathbf{q}^N))}$$

$$\equiv \frac{\int_1 \mathrm{d}\mathbf{r}^N \pi(\mathbf{r}^N)[R(\mathbf{r}^N, L_i) \exp(-\beta_i U(\mathbf{r}^N, L_i)/\pi(\mathbf{r}^N)]}{\int_1 \mathrm{d}\mathbf{r}^N \pi(\mathbf{r}^N)[\exp(-\beta_i U(\mathbf{r}^N, L_i)/\pi(\mathbf{r}^N)]}$$

$$\equiv \frac{\langle R(\mathbf{r}^N, L_i) e^{-\beta_i U(\mathbf{r}^N, L_i)}/\pi(\mathbf{r}^N)\rangle^{\pi}}{\langle e^{-\beta_i U(\mathbf{r}^N, L_i)}/\pi(\mathbf{r}^N)\rangle^{\pi}}; \tag{8}$$

once again we arrive at ratios of Monte Carlo averages easily collected during the run. This can be used to estimate both structural properties (such as pair correlations) and thermodynamic properties (such as pressure, internal energy or heat capacity). All of the first and second order canonical thermodynamics for the Lennard-Jones system were estimated using equation (8) in the present study (see Section 4).

However, it is, of course, possible instead to derive *all* of the canonical thermodynamic properties from $A^{\mathrm{Can}}(T,\rho)$, using temperature and density derivatives of the free energy, already estimated using equations (6) and (7). If the averages appearing in equation (6) are

collected for a fine regular grid of states (T_i,ρ_i) the numerical estimation of such derivatives is rather convenient. The thermodynamic properties were estimated in this way, as well as by direct averaging using equation (8); the relative efficiency of the two methods is of interest, and is discussed in Section 4. In the present study, we did not collect structural data [5,6].

2.2 Generating the sampling distribution $\pi(\mathbf{r}^N)$

The above is all formally correct for an *arbitrary* umbrella sampling distribution $\pi(\mathbf{r}^N)$. It is, of course, straightforward to use Markov-chain Monte Carlo methods to sample on *any* chosen $\pi(\mathbf{r}^N)$: it is only necessary [22] to choose a transition matrix $\tilde{\mathbf{p}}$ such that its elements satisfy

$$\pi((\mathbf{r}^N)_m)p_{mn} = \pi((\mathbf{r}^N)_n)\,p_{nm}. \tag{9}$$

However, practical success clearly depends on finding an *appropriate* sampling distribution, and this cannot be known *a priori*. The central challenge, therefore, concerns the efficient generation of a suitable $\pi(\mathbf{r}^N)$, apparently by a bootstrap procedure.

The requirements on $\pi(\mathbf{r}^N)$ are evident: (i) it must include all the parts of configuration space $\mathbf{r}^N$ relevant to *all* of the thermodynamic states (T_i,ρ_i) in the target region, and with roughly comparable weights for each (and, for efficiency, had better *not* include any large irrelevant regions of $\mathbf{r}^N$!), and (ii) the function $\pi(\mathbf{r}^N)$ should be moderately smooth over the whole relevant region, to ensure good "mobility", under the sampling algorithm, among the subregions relevant to the target states themselves. Following some preliminary remarks, we will discuss one approach to satisfying these requirements.

For simple one-dimensional scaling it is not difficult to generate an appropriate distribution π by brute-force numerical means. In the case of temperature-scaling at fixed density, for example, it is clear that one needs only to sample over a range of potential energy $U(\mathbf{r}^N)$ much wider than that characteristic of any single temperature, so one can use a distribution [1] which depends only on the potential energy: i.e. $\pi(\mathbf{r}^N) = \pi(U(\mathbf{r}^N))$. The form of π can be adjusted by trial and error to give a roughly uniform probability of potential energy over the required range (either by adjusting parameters in some simple functional form for $\pi(U)$, or by purely numerical adjustment of a histogram of π). Similar purely numerical techniques have been employed for Hamiltonian and order-parameter scaling (see [1,8,9 and 23]; the latter treatment is known as "multi-canonical sampling").

However, for two-dimensional thermodynamic scaling (TDSMC) such an approach would be difficult and tedious. Furthermore, the trial-and-error procedure would need to be repeated on moving to a system of different size N, and would become rapidly more demanding as N increased. A more sophisticated approach is required. We describe the approach used in the present study. It is effective, and also offers some general insight into choosing $\pi(\mathbf{r}^N)$.

This is based on expressing $\pi(\mathbf{r}^N)$ as a weighted sum of the Boltzmann distributions for a grid of states $k \equiv (T_k,p_k)$ spread through the two-dimensional target region:

$$\pi(\mathbf{r}^N) = \sum_k w_k \exp(-\beta_k U(\mathbf{r}^N, L_k)), \tag{10}$$

where w_k is the weight given to the k-th term. In the case of TDSMC, it is natural for the states to form a rectangular grid distributed uniformly in the target (T,ρ) region, for example; this was the choice in the present study. This choice will *not* sample irrelevant regions of the reduced configutation space, and if the grid of states k is sufficiently dense the overlap of their Boltzmann distributions in $\mathbf{r}^N$ will ensure the required reasonable smoothness of $\pi(\mathbf{r}^N)$—condition (ii) above. It remains to choose the weights w_k to satisfy condition (i), which is that each state be given roughly equal overall weight in the sampling.

However, it is clear that we will have equal overall weight for each state k if equation (10) is in fact the sum of *normalized* Boltzmann factors. In view of equations (4) and (6), this is equivalent to setting

$$w_k \propto \exp\left(+\beta_k A_k^{\mathrm{ex}}\right), \tag{11}$$

where A_k^{ex} is the excess free energy of state k. This looks good. The "catch" is that βA^{ex} is exactly the quantity we want to estimate! This emphasizes the inherently trial-and-error nature of generating an appropriate sampling distribution. But, it is in fact a happy realisation that, according to equation (11), the "best" weights w_k, in the present scheme, are given by a quantity we are anyway estimating: it means that we don't need to generate any *auxiliary* information in order to improve on a trial distribution $\pi(\mathbf{r}^N)$.

The refinement procedure is simple. Recall that estimates obtained using equations (4), (6) and (7) are in principle correct for any π. So, given a rough guess for the $\beta_k A_k^{\mathrm{ex}}$, and hence for $\pi(\mathbf{r}^N)$, we can use it to generate a *better* estimate of the $\beta_k A_k^{\mathrm{ex}}$—this estimate will be unbiassed (though possibly quite imprecise, of course). Thus it is easy to refine the sampling distribution in a few runs of modest length, before carrying out a longer "production run" to give accurate free energies throughout the target region.

Furthermore, once one has a reasonable estimate of βA^{ex} throughout the target region for a system of N_0 particles, one automatically knows a pretty good sampling distribution $\pi(\mathbf{r}^N)$ for a system of any other size N! That is because the excess *specific* free energy A^{ex}/N is, of course, almost independent of the system size N. (In these finite systems there is a small *real* N-dependence, of course; to account for this the new weighting function, obtained by appropriate scaling of equation (11) to the new size N, can be further refined by using a preliminary run as described above, although this is sometimes superfluous.)

So apparently, using equations (10) and (11), it is easy to bootstrap one's way to a good sampling distribution for a system of any size, only supposing one can find a barely usable guess of $\pi(\mathbf{r}^N)$ for an arbitrarily small system. But this is trivial, because of the breadth of Boltzmann distributions for small systems, and the relatively weak dependence of w_k on errors in the excess free energy for such systems. In fact, we find that, for a sufficiently small system, using in equation (10) one or a few states k, with any crudest guess for the w_k, will be adequate to start the bootstrap. (Alternatively one might perform a single canonical run for a state within the target region, estimating the energy and pressure and thus obtaining a linear approximation to the variation of $\beta A^{\,\mathrm{ex}}$ with temperature and density within the target region.) Of course, where a theoretical or computational estimate of A exists, however crude, one can likely begin with a system of reasonable size N; this was the case for Lennard-Jonesium, where the equation of state of Nicolas *et al.* [24], based on previous computational work, proved adequate to start a refinement process for π (within each of three subranges of the target density range) with $N = 72$.

This scheme for generating suitable sampling distributions worked smoothly in the present study, and in others we have since carried out. Evidently, the excess free energy $\beta_k A_k^{\mathrm{ex}}$ in equation (11) can be replaced by the *relative* excess free energy (relative to a constant reference state), the quantity actually estimated below. (It is only necessary to take care to calculate π in a way which avoids floating-point overflows, because the various contributions may range widely; e.g. in the case of $N = 500$, w_k turns out to vary over a factor of 10^{202} within the target region.) Further details are noted below.

Of course, the sum (10) must be calculated for each trial particle move. This requires some computing time (depending on the number of states k used in equation (10)) beyond that for the *single* Boltzmann factor required in a conventional single-state run, evidently. However, the computing effort is still dominated by calculation of the configurational sums which go into the trial energy $U(\mathbf{r}^N,L_k)$. With the current model (see below) the computing time per step necessary to generate the Markov chain is thus only moderately increased by the more complicated function π, from that of a conventional canonical Monte Carlo computation producing results for only a single state. (Of course, additional time is also associated with the mere filing of data for probably hundreds of states at each step, rather than for only one.) A modification of the above scheme, which reduces the computing time associated with computing the sum (10), is pointed out in Appendix A; this modification was not used in the present study.

2.3 Segmentation and other considerations

One may want to scan very large regions of temperature and/or density. For example, in the present study, in order to span the upper portion of the Lennard-Jones liquid–gas coexistence, we included in the target region reduced temperatures in a modest range (1.20–1.36), but necessarily covered reduced densities over a wide range: from 0.08 to 0.60, a ratio of 7.5; (these reduced variables are defined explicitly below). Now in principle (and in practice) one can cover in a single TDSMC run an *arbitrarily* large region. However, it is natural to ask whether this will be the most efficient strategy. That is because the Markov-chain sampling carries out a random walk; it is well-known that, in this case, for sufficiently large ranges the mean time necessary to traverse the range will go up as the square of that range. One might, therefore, expect the convergence and correlation times to get large where the range is very large, and the random error of the resulting estimates might then increase. If so, the efficiency might be improved by segmenting the target range into a few smaller ranges, overlapping at "seams", and each covered by a separate TDSMC run. If that is done, the free energy results can nevertheless be put on a common scale by "matching" their results at the "seams" where the subranges overlap. However, one doesn't want to subdivide the range too much, because this matching procedure will itself introduce additional uncertainties into the relative free energies, as well as being a complicated nuisance to handle during analysis of the data. So some sort of trade-off sounds desirable, attempting in a rough way to optimize some mixture of computing efficiency and human patience.

With this in mind, the present study was actually duplicated: (i) it was carried out by segmenting the overall density range into *three subranges* (specified in the next subsection) and carrying out TDSMC runs in each of these subranges separately (the procedure is here denoted "3S"), and then (ii) also carried out independently by covering the entire target range in *one big* TDSMC run (denoted "OB"). In the former case (3S), the resulting relative free energies were put on a common scale by comparing results along the two "seam" densities at which the segments overlapped. The excellent agreement of the thermodynamic results of these two independent studies is pointed out below, and was of course, very reassuring. What was more surprising, however, was to find that for comparable amounts of computing their standard errors were roughly the same throughout the target range in the two investigations. (Explicit comparisons of the two sets of results are shown below in several places.)

If this insensitivity of the error to segmentation turned out to be generally true, there would be a strong argument for using only *one big run* (OB), covering the whole range. That is because one gains relief from the considerable extra complication in analysis that is associated with "matching" the subrange results at the "seams", and especially in making a proper estimate of the resulting contributions to the error (as pointed out below and with greater detail in Appendix B). It might be thought, against this, that generating an adequate

sampling distribution for the larger range would be more demanding; this is not really true, however, since if one is able to generate useful sampling distributions for the separate segments it is no extra effort to patch them together to cover the full target range. In retrospect, therefore, use of a single TDSMC run (OB) was preferable in the present case.

All of the main thermodynamic results reported in what follows are derived from the OB investigation, but direct comparisons with those from 3S, and of their respective errors, are made in several places.

Although, as remarked, the computing time required for each Monte Carlo *step* is only modestly increased from that for conventional work on fluids, one must still worry about the *total* computing demands. In each TDSMC run one can collect data for an arbitrarily large number of thermodynamic states (T,ρ) in the target region—in the present study, this was done for 901 states when using a single run (OB), and correspondingly several hundred in each subrange when the study used segmentation of the target range (3S). To get good data for so many states requires, not unexpectedly, runs longer than for a conventional single-state Monte Carlo run. The surprise is that the required runs are not so very much longer, so the TDSMC computation is in a sense extraordinarily efficient. (For $N = 500$ the production run for OB required about 73 h on a 500 MHz Alpha CPU, producing results for 901 ($T*, \rho*$) states: about 5 min for each state. (Actually almost half of that time was used in calculating quantities required for "direct" calculation of canonical averages (8) and the filing of such results for all the target states; it is argued below that this is completely pointless, because equally satisfactory results are accessible simply by differentiating the relative free energies.)) One basic reason for this apparent efficiency is of course that in principle *each* sampled configuration contributes to the required averages at *every* thermodynamic state; in practice, each configuration makes a *substantial* contribution only to a more limited range of states, but enough to look remarkably efficient. At the same time, the "tails" of the distributions for individual states, poorly sampled in conventional single-state work, are automatically well-sampled in TDSMC, which must be part of the explanation for the remarkable precision in the results which we report below.

The "downside" of this apparent efficiency is of course that the results for nearby thermodynamic states are necessarily correlated. This means that the estimation of statistical errors in the results requires some care. For example, in estimating the random error in the relative free energy between two states we must take into account not only the variances of the separate averages for each, but also any covariance. This is mentioned below in the context of the present study, and detailed in Appendix B, where the (considerable) extra complication of free energy error estimation resulting from the "seams" between subranges, if the target region is segmented (as in 3S), is also made explicit.

2.4 The model and further details

In order to demonstrate the implementation of TDSMC, it has been applied to the Lennard-Jones fluid, over a target range (T,ρ) which includes the critical point of its liquid–gas transition. This model is described by an energy parameter ε and a distance parameter σ. It is convenient to specify the thermodynamic states in terms of reduced temperatures $T_i^* \equiv k_B T_i/\epsilon$ and reduced densities $\rho_i^* \equiv N\sigma^3/V_i$. Then the potential energy of the system, $U(\mathbf{r}^N,L_i)$, is the sum of Lennard-Jones pair potentials, and at (T_i,ρ_i) is given by

$$\beta_i U(\mathbf{r}^N, L_i) \equiv \frac{U(\mathbf{r}^N, L_i)}{k_B T_i} = \frac{4}{T_i^*}\left[\sum_{m<n}\left(\frac{\tilde{\sigma}_i}{r_{mn}}\right)^{12} - \sum_{m<n}\left(\frac{\tilde{\sigma}_i}{r_{mn}}\right)^{6}\right], \quad (12)$$

where r_{mn} is the separation of particles m and n (in the reduced unit-volume configuration space (3)), and $\tilde{\sigma}_i$ is the reduced σ-parameter appropriate to the density ρ_i:

$$\tilde{\sigma}_i \equiv \frac{\sigma}{L_i} \equiv \left(\frac{\rho_i^*}{N}\right)^{1/3}. \quad (13)$$

As usual the pair-interactions in equation (12) were truncated at a spherical cut-off, and tail corrections were subsequently added. In the results reported below, the cut-off was equal to half the box length; this is a popular and convenient choice, but alternatives such as a constant *physical* cut-off length (hence a density-dependent cut-off in the reduced coordinates) could equally have been chosen (such "truncated" Lennard-Jones models have been studied by several authors, including for example, [25]. In the case of the relative free energy, this means modifying equation (6) to read

$$\frac{\beta_j\left(A_j^{\mathrm{ex}}\right)^{\mathrm{Can}}}{N} - \frac{\beta_i\left(A_i^{\mathrm{ex}}\right)^{\mathrm{Can}}}{N} = \frac{1}{N}\log\left(\frac{Z_i^{\mathrm{ex}}}{Z_j^{\mathrm{ex}}}\right) + (\mathrm{tail})_j - (\mathrm{tail})_i, \quad (14)$$

where $(\mathrm{tail})_i$ is the tail correction appropriate to $\beta_i A_i/N$, and the averages in $Z_i^{\mathrm{ex}}/Z_j^{\mathrm{ex}}$ (equation (14)) have been calculated using the truncated potentials. Where other thermodynamic properties were calculated "directly", using equation (8), an appropriate tail correction has to be added to that equation. The tail corrections were calculated assuming a unit pair correlation function beyond the cut-off; the details of the tail corrections required for each property are given in [7].

Each step was like that of a conventional canonical Monte Carlo calculation. That is, it consisted of a uniformly random trial move of a randomly-chosen particle, within a local region of the reduced space (centred on that particle's old position), followed by acceptance or rejection to satisfy equation (9). The only difference lies in the more complicated form (10) of $\pi(\mathbf{r}^N)$. (For the particular model, this is not at all onerous,

because the updating of the two sums $\sum_{m<n}(r_{mn})^{-12}$ and $\sum_{m<n}(r_{mn})^{-6}$, including all $r_{mn} < 0.5$, is sufficient (cf. (12)) to give the new energy for *every* target state (T_i,ρ_i), and thus for every term in $\pi(\mathbf{r}^N)$. This is exactly the same geometrical calculation required in a conventional canonical single-state simulation. (This extreme economy is partly an accident of the cut-off choice, of course, since each of the two sums required is identical for all densities: they simply require scaling by the appropriate powers of $\tilde{\sigma}_i$ for each density ρ_i. With a *constant* physical cut-off length, by contrast, the sums at various densities must involve *different* cut-offs when expressed in reduced coordinates, and so different selections of the pair interactions: those for which the pair separation is less than the reduced cut-off appropriate to the density. This makes the energy calculations very slightly slower, since one must keep track of these selections.)

The basic study covers the temperatures T_i^* from 1.20 to 1.36 (or to 1.40 for $N = 72$) and densities ρ_i^* from 0.08 to 0.60; the target region was chosen to include the upper part of the liquid–gas coexistence region. For this region, we report results for $N = 72$, 256 and 500 particles. Data on free energy and other properties was extracted for a rectangular grid of states, separated by intervals of 0.01 in both T_i^* and ρ_i^*, thus for 901 thermodynamic states in all (or 1113 for $N = 72$). For each state we estimated the averages (cf. (7)) necessary to give its relative free energy, and also those (cf. (8)) required to calculate directly (reduced forms) of the mean potential energy $\langle U\rangle^{\mathrm{Can}}$, the pressure p^{Can} (from the mean virial of forces), and (by averaging fluctuations and the correlation of energy and pressure) the heat capacity C_v^{Can}, the inverse compressibility $(k_T^{\mathrm{Can}})^{-1} = -V(\partial p^{\mathrm{Can}}/\partial V)_T$ and the internal pressure $p_{\mathrm{int}}^{\mathrm{Can}} = -(\partial\langle U\rangle^{\mathrm{Can}}/\partial V)_T$. (Explicit formulas can be found in [7].)

The sampling disribution was that of equations (10) and (11). For convenience, the states k included in π matched (half of) those for which data was being collected, as described above (but skipping alternate temperatures: i.e. the k states occurred at intervals of 0.02 in reduced temperature, but 0.01 in $\rho*$). (Of course, there is no need to match in any way the states k included in π with those for which data is collected—this is merely convenient. Also, this density of states k is certainly unnecessarily large, especially for the smaller N, but no attempt was made to optimize in this respect.)

As mentioned above, the full target range was studied (for each system size N) in two different ways: either using *one big* TDSMC run (OB), or by segmenting into *three subranges* (3S) and doing a separate TDSMC run on each. In the latter case (3S), the data presented result from choosing the reduced density subranges 0.08–0.20, 0.20–0.40 and 0.40–0.60 (collecting data at 221, 357 and 357 thermodynamic states, respectively, more for $N = 72$). Along the "seams" at $\rho* = 0.20$ and 0.40 there are derived sets of excess reduced free energies from each of two runs, *relative to* an arbitrary reference state for each. Of course, these reference states will differ for the adjoining runs. But comparing the two sets of data along the seam allows one to estimate the constant necessary to put the free energies of the adjoining subrange runs on a common scale, and also to estimate the error associated with this matching procedure. To be more explicit, two adjacent runs will each give the reduced excess free energies relative to that of some arbitrary *local* reference state; what is then still needed is the difference between the excess free energies. of the two *reference* states. This was estimated by the difference (between the runs) of the means of the reduced excess free energies for all the states along the seam. This choice of estimator minimizes the mean square deviation between the two sets of results along the seam (after putting them on a common scale), and this deviation in turn contributes to the estimated uncertainty of relative free energy for states on opposite sides of the "seam"—the details are described in Appendix B. Such complications are of course, avoided in the OB realisation.

Table 1. Thousands of MC steps per particle.

Version	*OB*	*3S*			
ρ^* *range*	*0.08–0.60*	*0.08–0.20*	*0.20–0.40*	*0.40–0.60*	*Total*
$N = 72$	4306	667	1000	833	2500
$N = 256$	1367	375	750	375	1500
$N = 500$	1440	240	768	576	1584

Table 1 gives the length of the Monte Carlo runs used to produce the results cited, in each case several hundred thousand steps per particle. It may be noted that the *total* number of configurations used was similar for the OB and 3S investigations, at least for the two larger systems.

3. Relative free energies

The relative excess free energy embodies in principle complete thermodynamic information throughout the region of temperature and density for which it is known. The most basic results of the TDSMC investigation are, therefore, the estimated relative reduced canonical excess free energies for states within the target (T,ρ) range. Figure 1 shows these data, for the case $N = 500$, in the form of differences of this quantity for the states i, at (T_i^*, ρ_i^*), from that at a reference state of $T_{\mathrm{ref}}^* = 1.20$, $\rho_{\mathrm{ref}}^* = 0.08$:

$$\Delta\left(\frac{\beta_i A_i^{\mathrm{ex}}}{N}\right)^{\mathrm{Can}} \equiv \left(\frac{\beta_i A_i^{\mathrm{ex}}}{N}\right)^{\mathrm{Can}} - \left(\frac{\beta_{\mathrm{ref}} A_{\mathrm{ref}}^{\mathrm{ex}}}{N}\right)^{\mathrm{Can}}; \qquad (15)$$

here and elsewhere this Δ, without a subscript, indicates differences from a common reference state, as described.

What has actually been plotted in figure 1 is straight-line segments joining the adjacent data points along each isotherm. The fact that the isotherms look like smooth curves is due to (i) the many thermodynamic states for which data was collected: 53 along each isotherm, and at the same time to (ii) the high precision of the data. It is

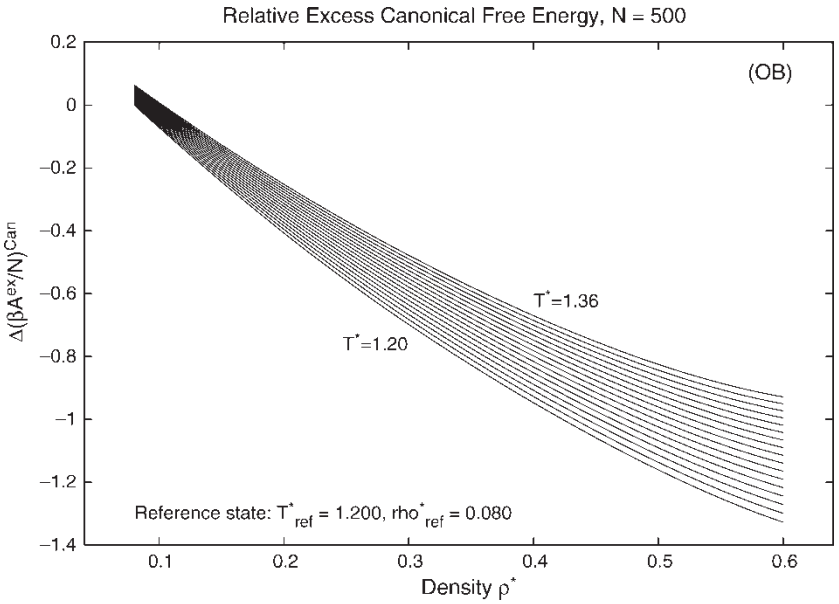

Figure 1. Relative reduced excess Helmholtz free energy as a function of density in the OB investigation, for $N = 500$, along the 17 isotherms for which data was collected. Along each isotherm the data is plotted as straight-line segments joining the raw estimates.

worth emphasizing this precision, because it makes possible quite surprising applications of the data (below and in the following paper [19]).

A rather careful error analysis was carried out (as described in Appendix B). The estimated errors would be invisible in figure 1. Instead, figure 2 shows the apparent standard deviation of the data in figure 1 (but on a scale expanded by a factor of 2500) along three of the isotherms and over the whole target density range. As expected, the error rises very roughly as the root of the separation from the reference state. What is striking, however, is its small magnitude: even for the most extreme separation of states—corresponding to a density *ratio* of 7.5—the standard error appears to be less than 0.0006 (that is in a quantity of order unity, so it's well under 0.1%)! Elsewhere, the standard error is still smaller. It is this remarkable precision which allows elaborate numerical manipulation of the data, to extract other properties and detailed phase-transition information, as we will see; e.g. it allows decent numerical differentiation, even useful second derivatives.

Figure 2 shows the apparent errors for both the one-big-run (OB) and three-subrange (3S) studies. There is little difference. Since (cf. table 1) the two versions used comparable total numbers of Monte Carlo steps (for $N = 500$), the computing efficiency turns out to be remarkably similar in the two cases, as mentioned above.

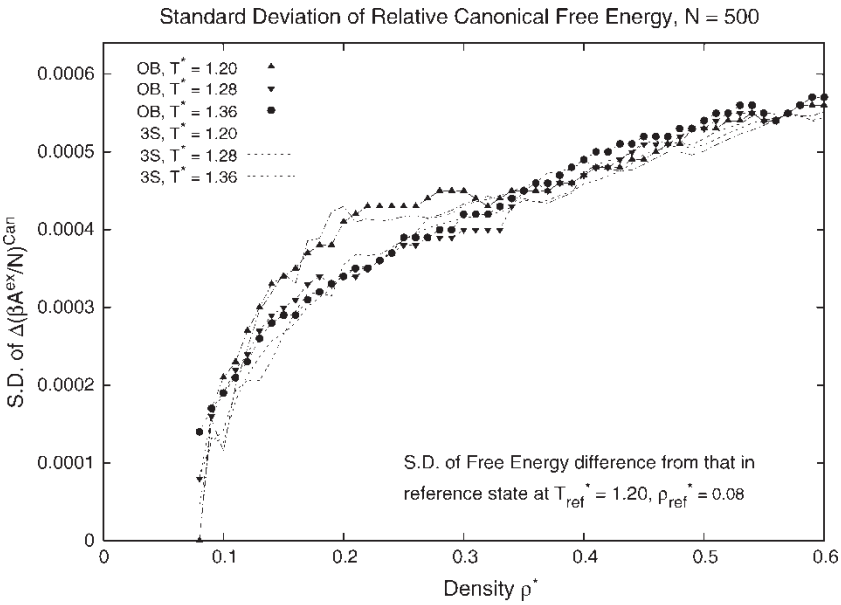

Figure 2. Apparent standard deviation of the relative reduced excess Helmholtz free energies (as shown in figure 1), along three of the isotherms. The figure also shows similar standard deviations from the segmented (3S) investigation: there is little difference.

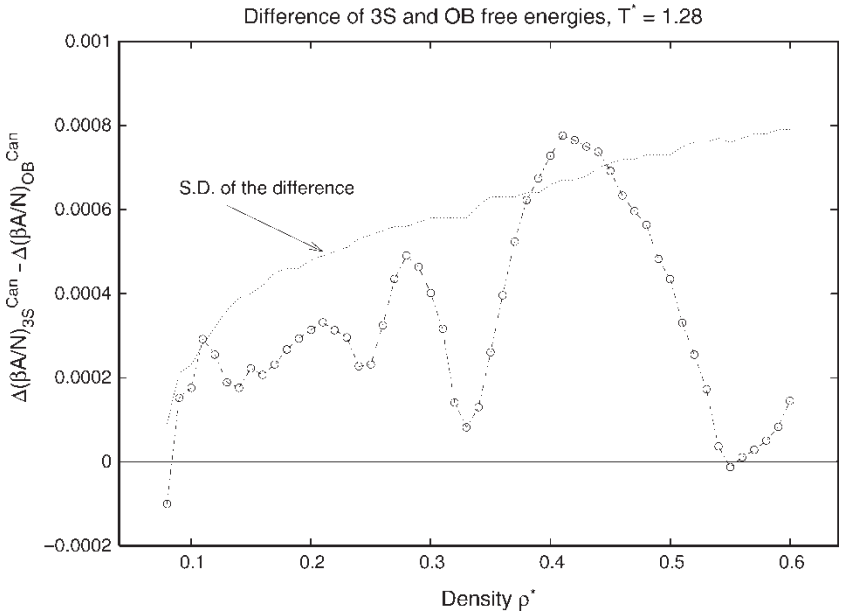

Figure 3. Difference between the estimates of relative Helmholtz free energy in the OB and 3S investigations, for $N = 500$, along a sample isotherm (open circles). The figure also shows (solid curve) the apparent standard deviation of this difference calculated from those of the separate investigations.

The analysis of the 3S study, which involves matching of subrange runs at the two seams, is considerably more complicated to carry out (cf. Appendix B and the following section), so there is a strong argument for using OB, at least in the present case, provided this insensitivity of the computing efficiency extends to the other properties.

The results shown in figure 1 are actually those for the OB study. In agreement with the small estimated errors, the OB and 3S free energy results are completely indistinguishable on the scale used in figure 1. We look at this more closely in figure 3 by showing the actual *differences* of the 3S and OB results along an isotherm; the apparent standard deviation of the difference is calculated from those of the separate independent results in the two cases. It is apparent that the differences between these independent investigations are indeed consistent with the apparent statistical errors; this is the case at all the target temperatures.

Of course, we obtain the relative reduced free energy itself by adding the relative ideal free energy (cf. equation (5)). Figure 4 shows some raw results, again showing differences from the same reference state and again plotted as straight-line segments joining adjacent

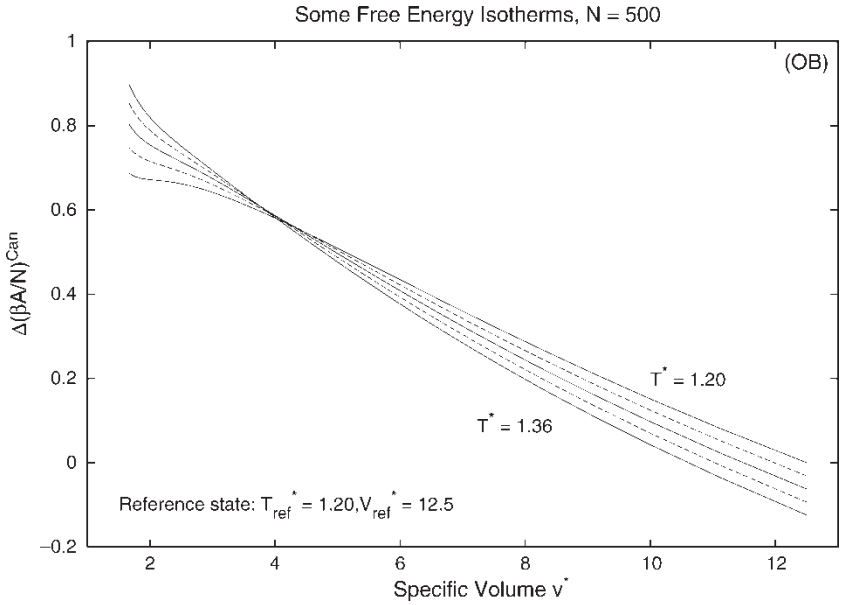

Figure 4. Relative reduced total Helmholtz free energies plotted as a function of volume for five equally-spaced isotherms, $N = 500$. The shapes reflect the liquid–gas phase transition.

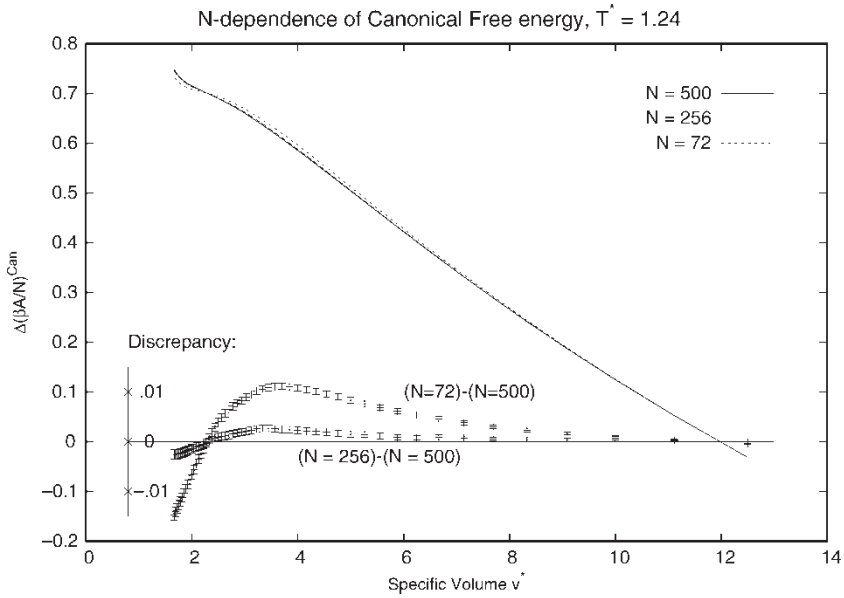

Figure 5. Relative reduced Helmholtz free energy along a sample isotherm for three sizes: $N = 500$, 256 and 72. The *differences* of the $N = 256$ and $N = 72$ free energies from those of $N = 500$ are shown in an inset, on a scale expanded by a factor of ten, and including error bars showing the standard deviations of the differences.

data-points along each isotherm. For clarity, results have been plotted along only five (equally-spaced) isotherms, of the seventeen studied. They have been plotted as a function of the reduced volume $v* \equiv 1/\rho*$. One can see that at the highest temperature the isotherm is everywhere convex, but at lower temperatures the isotherms contain a concave portion. The latter signals a first-order phase separation (the liquid–gas transition), and from the isotherm can be derived the densities of the coexisting phases and the vapour pressure (cf. Section 5).

The results are systematically different for different system sizes N. Figure 5 shows the relative free energy with $N = 72$, 256 and 500, at a typical subcritical temperature, $T* = 1.24$. The differences due to size N are sufficiently small that they are not easy to survey on the free energy curves themselves. These differences are therefore plotted on an expanded scale ($\times 10$) below, along with the estimated uncertainties (of the differences). While the N-dependence is small at low densities (high volumes), it becomes more substantial at higher densities; in particular, the N-differences are much bigger than their uncertainty, so that rather detailed study of the N-dependence of the thermodynamics of small (periodic) systems is accessible; we do not pursue this aspect further here. (These displayed N-dependences are quite distinct, of course, from the artificial N-dependence of the free energy of finite systems associated with truncation of Stirling's approximation, since that effect cancels out in these *relative* free energies.)

In much of what follows we use direct numerical manipulation of the free energy data described above. An alternative way of exploiting the data is of course to fit them by an algebraic expression, which can then be manipulated algebraically. We have also done this, and we later compare this with the more direct numerical analysis of our data; the following paper [19] makes extensive use of such fits.

For this purpose the variation of the estimated relative *excess* free energy (15) (relative to the reference state specified above) was fitted (for each system size N) according to

$$\Delta\left(\frac{\beta A^{\mathrm{ex}}}{N}\right)^{\mathrm{Can}} = \frac{\sum_{p=0}^{n_t}\sum_{q=0}^{n_d} a_{p,q} x^p y^q}{1 + \sum_{p=0}^{n_t}\sum_{q=0}^{n_d} b_{p,q} x^p y^q}, \qquad (16)$$

where $x \equiv T_i^* - T_{\mathrm{ref}}^*$ and $y \equiv \rho_i^* - \rho_{\mathrm{ref}}^*$ (and with $a_{0,0} = 0$). Where we report results involving such fits, we have used those for $n_t = 4$ and $n_d = 5$, i.e. the 901 data points (or 1113 for $N = 72$) are fitted using 59 parameters; the fits appear similarly good, however, as long as n_t and n_d are at least 3. We refer to such an algebraic fit as an "A-fit".

Of course the fitted free energies would be indistinguishable from the original data directly obtained using equation (7), on plots of the reduced free energy. Instead a plot of the *difference* of the A-fit from the original data is in figure 6. The figure shows as well (plus and minus) the standard deviation of the direct estimates: it is clear that the fit meanders comfortably within that envelope. This figure is for a particular temperature ($T* = 1.28$) and size ($N = 500$), but is typical of the goodness of fit for other temperatures and sizes. It is naturally very convenient to derive further thermodynamic properties by using these algebraic fits to the free energy as an alternative to more direct use of the computational data; we will look at some results of this kind below. Presumably an additional benefit is that they will tend to smooth out local fluctuations in the results between nearby (T,ρ) states. On the other hand to

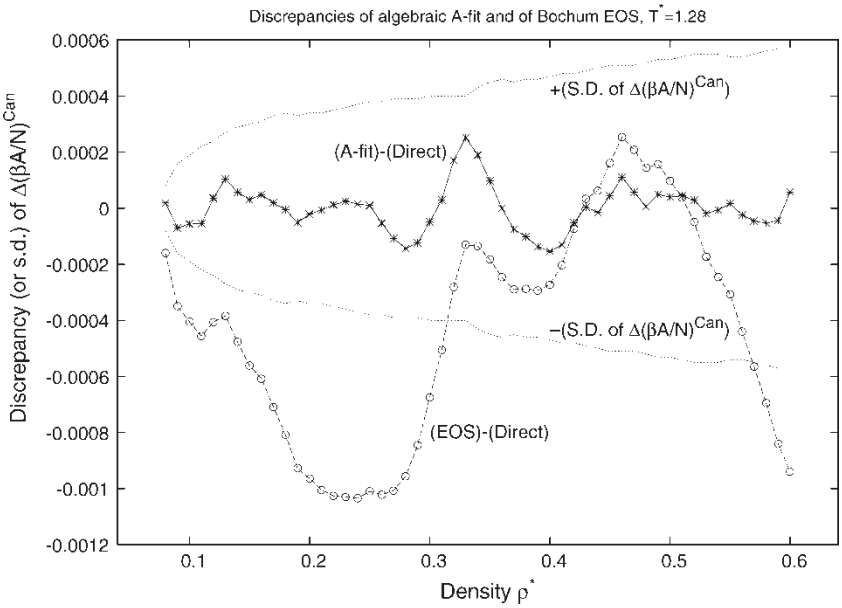

Figure 6. Differences, along a typical isotherm for $N = 500$, from the relative free energy determined "directly" in the (OB) TDSMC run; this shows (stars) the differences of the algebraic "A-fit", and also (open circles) of the equation of state due to Mecke *et al.* [27]. The dotted curves show plus and minus the standard deviation of the directly-determined free energies.

determine the propagation of errors in the derived results becomes difficult. To make some of our free energy results more directly accessible, we give in table 2 the fitting parameters $a_{p,q}$, $b_{p,q}$ for the $n_t = 4$, $n_d = 5$ A-fit to the relative excess free energy for $N = 500$.

There exist several published algebraic equations of state for (this version of) Lennard-Jonesium [26,27], based essentially on analysis of large amounts of energy and pressure data from the simulations of several groups. One of the best such equations is due to Mecke *et al.* [27], who give an explicit formula for the excess free energy which we refer to as the "Bochum EOS". This prediction is also displayed in figure 6, again as the discrepancy from our results. It is in remarkably good agreement, especially in view of the fact that simulation results for systems of various sizes were used in deriving the equation of state; the close agreement through the density region of macroscopic instability is, therefore, presumably partly fortuitous. (In spite of this good agreement, the rapid variation of the discrepancy with density might mean noticeable differences in derived thermodynamic properties and particularly in coexistence parameters.) By contrast, the equation of state of [26] shows a discrepancy rising to 0.009 over this density range at this temperature.

4. Other thermodynamic functions

In this section, we describe the data on various thermodynamic functions other than the Helmholtz free energy. Throughout we refer to states determined by the values of (N,V,T), and the thermodynamic functions are

Table 2. Parameters of free-energy fit "A-fit", $N = 500$.

	p = *0*	*1*	*2*	*3*	*4*
			Coefficients $a_{p,q}$		
q = 0					
0	0.0000000	0.49821633	82.626442	822.15918	8451.4678
1	−3.8502352	−642.83905	−6345.5386	−67208.742	12019.867
2	23.305815	2717.1179	31338.564	239144.69	−120967.09
3	−93.658577	−8048.5879	−69483.883	−801060.38	1042652.7
4	65.016975	3155.2456	35068.188	770754.94	−2150482.8
5	31.343840	3187.0090	−25291.100	−162900.48	1960966.6
			Coefficients $a_{p,q}$		
0	0.064154409	178.99205	1945.6906	20331.174	19172.648
1	−5.8638544	−675.87354	−8154.1172	−66532.805	−21389.771
2	22.035810	1962.8533	14519.366	213439.52	−124508.08
3	0.36127260	406.61880	14751.100	−46042.320	771946.12
4	−26.036913	−2068.1433	−29934.820	−245485.66	−791633.62
5	2.1773016	683.68701	33982.102	278437.12	−46451.820

those within the canonical ensemble. (Of course the ensemble doesn't matter in the thermodynamic limit, but here we are examining rather small finite systems for which the (finite-system analogues of the) thermodynamic functions differ somewhat for the various ensembles. It is, therefore, important to have the distinction in mind.)

As we have pointed out, the thermodynamics can be derived in various ways from the results of a TDSMC investigation. Most directly, the mean thermodynamic functions can be expressed in terms of canonical averages, sometimes of fluctuation quantities; the required formulas and the associated tail corrections may be found in [7]. These canonical averages can be estimated in turn using equation (8), by collecting for each property the two π-averages required; this is to be done for an arbitrarily large set of thermodynamic states within the target range—in the present case for 901 different states. This we call the "direct" method. Alternatively, having derived the reduced *free energy* throughout the target range (using equations (6) and (7)), the other thermodynamic functions can then be derived by estimating the various required temperature and density derivatives of the free energy, using numerical differentiation—this is the "derivative" method. It will be useful to compare the efficiencies of these two approaches. A third possibility is to generate the thermodynamic functions by algebraic differentiation of the *fit* to the free energy in the target range, described above—the "A-fit" method. In addition, as noted, the entire investigation was carried out twice, using independent simulations: once segmented into three runs covering subranges of density (3S), and again in one big run (OB). We thus wish to evaluate a large number of routes to the thermodynamic quantities.

To obtain the first and second order differentials of the reduced free energy required in the "derivative" method, the numerical differentiation could be carried out in various ways. The simplest, or "three-point", estimates (cf. e.g. [28]), involving the estimated free energies at only three adjacent states (or nine in the case of the mixed second-derivative), turned out to be quite adequate for the present purpose, in the sense that the resulting derived thermodynamic functions agreed with those of the "direct" determinations within, and usually well within, the estimated error of either estimate, as we will see. This is a consequence of the remarkable precision of the free energies. We therefore report in what follows, except as noted, only such "three-point" estimates (which are in error beginning with cubic contributions to the local variation of free energy). One could use more sophisticated numerical estimates—even just the "five-point" differentiation formulae—but this would render the estimation of the uncertainties in the derived quantities more involved; in view of the fact that the results already agree well within the apparent errors this didn't seem worthwhile (except as noted below). Each differential appears as a linear combination of adjacent relative reduced free energies, and the uncertainties are, therefore, readily calculated from the variances of and the covariances between the estimates of these free energies. In order to obtain these, the run was regarded as consisting of a series of sub-runs, or "cycles" and various averages for each of these cycles for each state were stored during the run; these were tested (and where necessary combined into longer sub-runs) to ensure the required lack of correlation between the cycle averages. An analysis programme was written which calculates all the required mean free energies and all the necessary variances and covariances, and hence the "derivative" thermodynamic quantities and their uncertainties, directly from the stored "cycle" averages of the required π-averages which appear in equation (7). (At the boundaries of the target region it is of course necessary to use "one-sided" estimates of the differentials, rather than the symmetrical versions [28], with a consequent loss of accuracy. For the density-derivatives at the "seams", in the 3S investigation, it is easy instead to decompose the formulae into terms from each of the adjoining runs.)

We begin with (Subsection 4.1) the first-order quantities, i.e. internal energy and pressure (derived from simple averages of mechanical quantities, or requiring only first-order derivatives of free energy), then go on to (Subsection 4.2) the second-order quantities (which depend on averages of fluctuation quantities, or on second derivatives), adding some remarks (Subsection 4.3) on other thermodynamic functions to be derived from the above.

4.1 First-order thermodynamic functions

The reduced mean internal energy per particle $\langle \beta E/N \rangle^{\mathrm{Can}}$ is made up of the reduced mean potential energy, $\langle \beta U/N \rangle^{\mathrm{Can}}$, and the corresponding reduced kinetic energy, which has the value 1.5. The reduced mean canonical potential energy can be estimated "directly" from equation (8) by setting R to be the reduced potential energy of the system (using the truncated potential, and afterward adding the tail correction), or alternatively in the "derivative" approach by noting that

$$\langle \beta U/N \rangle^{\mathrm{Can}} = -T* \left(\frac{\partial}{\partial T*} \Delta \left(\frac{\beta A^{\mathrm{ex}}}{N} \right)^{\mathrm{Can}} \right)_{\rho*} . \qquad (17)$$

The mean potential energies for all 901 thermodynamic states are shown in figure 7 (again as straight line segments joining adjacent values along each isotherm). (These are in fact OB results using the "direct" determination, but results from other routes are indistinguishable on this scale.) Apparent standard deviations are shown in the insert (for only one temperature, but the results are typical) on a scale expanded by a factor of 100, for both the "direct" and "derivative" estimates and for both OB and 3S investigations. Clearly, there is again *no* systematic difference of precision between the various ways of

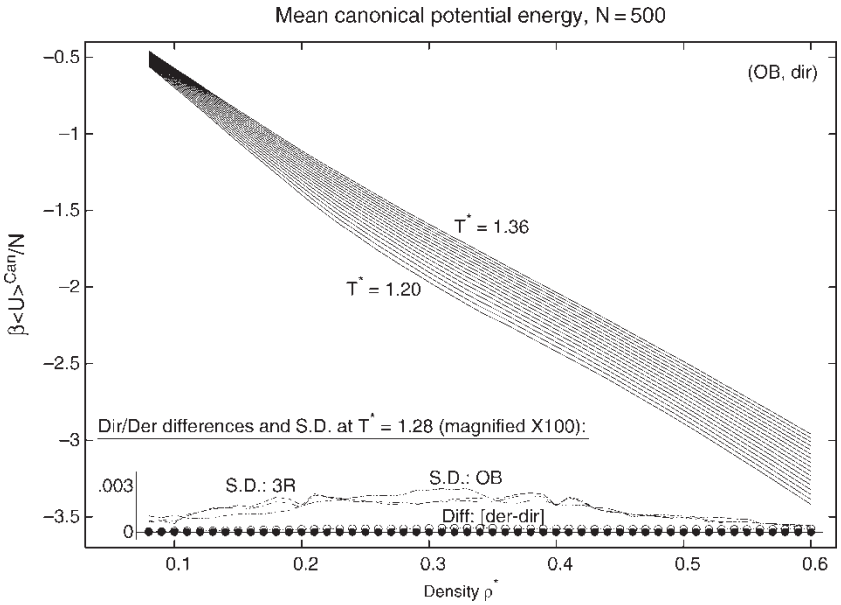

Figure 7. The mean reduced potential energies are shown for all 901 thermodynamic states, again plotted (cf. figure 1) as straight-line segments joining adjacent points along each of the 17 isotherms. The inset shows, for a typical isotherm, on a scale expanded by ten, the differences between the energies derived by the "direct" and "derivative" routes, both using 3-point (open circles) and 5-point (dark circles) estimates of the derivatives. Also shown there are estimates of the standard deviations from both the OB and 3S investigations: once again there is little to choose between them, and the difference between the "direct" and "derivative" routes is small compared to the uncertainty of either.

estimating the energy. (The dips in the standard deviations in the 3S case, precisely at the "seams", arise because at these densities sampling is available from both of the adjoining subrange runs.) The precision of these energy estimates is very pleasing. Also shown are the differences between the "direct" and "derivative" estimates in the OB case, using the "three-point" differentials (open circles): we see that the differences are very small compared to the standard deviations of either, so the two estimates are equally useful. (At the same time, it is evident that there is a tiny *systematic* difference, presumably due to inadequacy of the "three-point" formula for the numerical derivative. Indeed, if the "five-point" estimate is used instead (black circles), this discrepancy disappears. However, this is relevant only for the potential energy: for the other properties this subtle effect is lost in the noise, and we revert to the "three-point" estimates.)

The energy results in figure 7 are actually from the single-run (OB) investigation, obtained by "direct" averages. It is worth checking that energies estimated in the OB and 3S investigations actually agree with each other. The *difference* of the estimates (at $T* = 1.24$ as an example) is shown in figure 8; since the OB and 3S runs were independent, the distribution of the differences should be described by a standard deviation easily calculated from those of the separate results, and shown (plus and minus) on the figure. We see that the observed differences are indeed consistent with that (very small) standard error, and furthermore seem random as to sign, confirming the equivalence of the two investigations. The figure shows also the difference of energies derived by algebraic differentiation of the fit of the free energy described earlier: the A-fit. It is important to recall that that fit was strictly to the *free energy*, not a fit to the energy itself. Nevertheless one might hope that the derived energies would differ from the energies obtained directly as canonical averages (cf. (8)) by amounts at most comparable to the errors in the latter estimations, and we see that this is indeed the case; the results derived from the A-fit are no doubt a "smoothed" representation of the results.

The number-dependence of the mean potential energies is quite noticeable at densities near those of the phase transition. This is demonstrated for a few temperatures in figure 9. (It should be recalled (cf. figure 7) that the errors in these estimated energies are comparable to the line thicknesses.) The figure also compares our $N = 500$ energy results at $T* = 1.30$ with high-quality data due to Kolafa *et al.* [29]. The agreement is really excellent (though outside the combined estimated errors at a couple of the lower densities); the estimated standard errors [29] are from 1 to 4 times as great as in the present investigation. Some results for $N = 256$ at $T* = 1.20$, from an earlier study, are also shown.

The pressure can be estimated "directly" by finding the mean virial of forces, using equation (8) (adding the appropriate tail correction), and thus the excess pressure, or from derivatives of the free energy by noting

$$\beta\sigma^3 p^{\mathrm{Can}} = \rho* + (\rho*)^2 \left(\frac{\partial}{\partial \rho*} \Delta \left(\frac{\beta A^{\mathrm{ex}}}{N} \right)^{\mathrm{Can}} \right)_{T*}. \qquad (18)$$

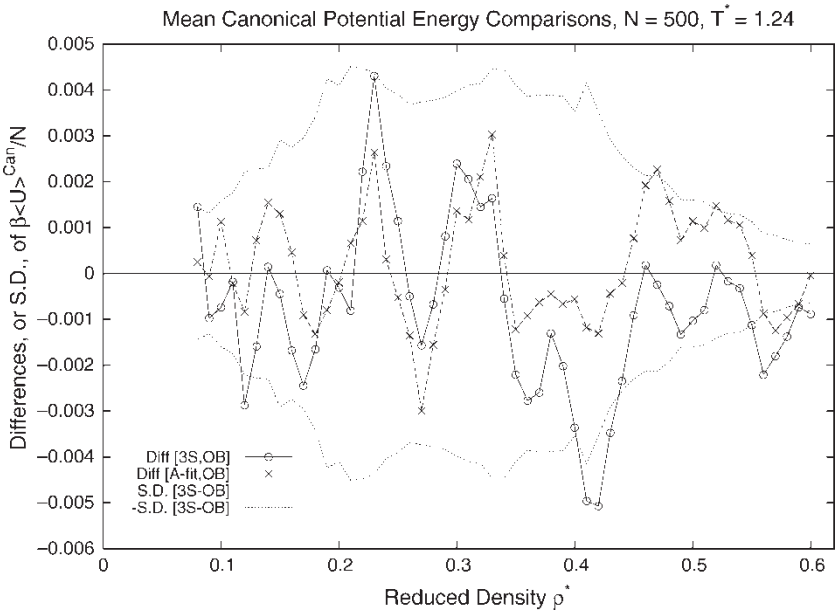

Figure 8. Differences from energies determined in the OB investigation of those from the 3S investigation (open circles) and also of those derived from the fit "A-fit" to the free energies (crosses), along an isotherm. The solid curves show, for comparison, the apparent standard deviation of the 0B−3S difference.

The pressures are shown (black dots) along each isotherm in figure 10, for $N = 500$ (OB, deriv). Along five of the isotherms error bars are shown (one standard deviation); they are satisfactorily small. The solid curves show the pressure calculated by algebraically differentiating the free-energy fit, A-fit. Although that fit was to the free energy only, these pressure results are clearly quite accurate; (a possible exception is precisely at the highest density, $\rho* = 0.60$, where some of the fits appear to be slightly outside the standard deviations—of course it was necessary on this boundary to use the less accurate asymmetrical or "one-sided" numerical estimate of the derivative). At low temperatures the "Van der Waal's loop" associated with the liquid−gas coexistence is evident, while at the higher temperatures the curves are monotonic.

For a single temperature, by way of example, we examine more closely the estimated standard deviations in the pressure for both the OB and 3S investigations, and using both the "direct" and "derivative" methods. These are compared on an expanded scale (× 25) in the inset: it is again clear that there is little to choose between the

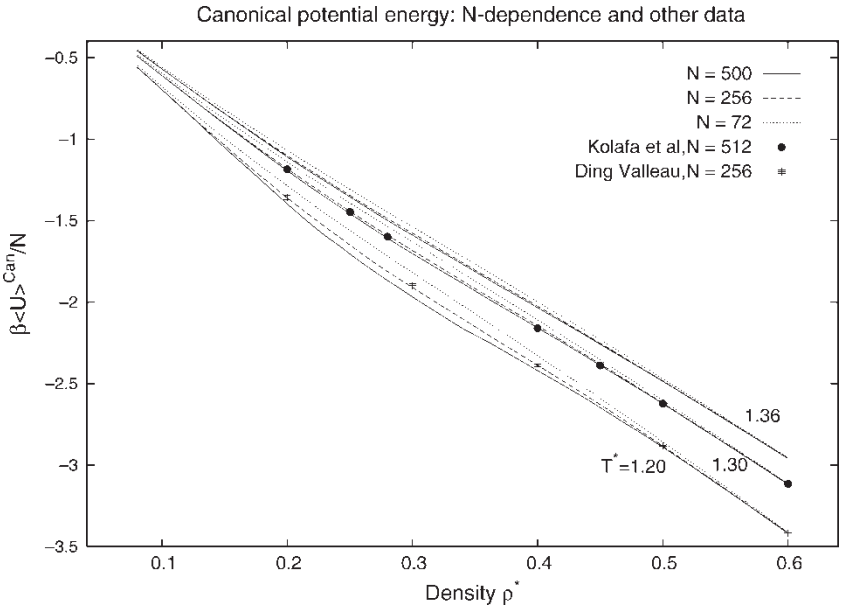

Figure 9. Mean potential energies along three isotherms for various sizes N. The N-dependence is large in the coexistence region, and remains substantial at supercritical temperatures near the critical density. Some previous results are shown.

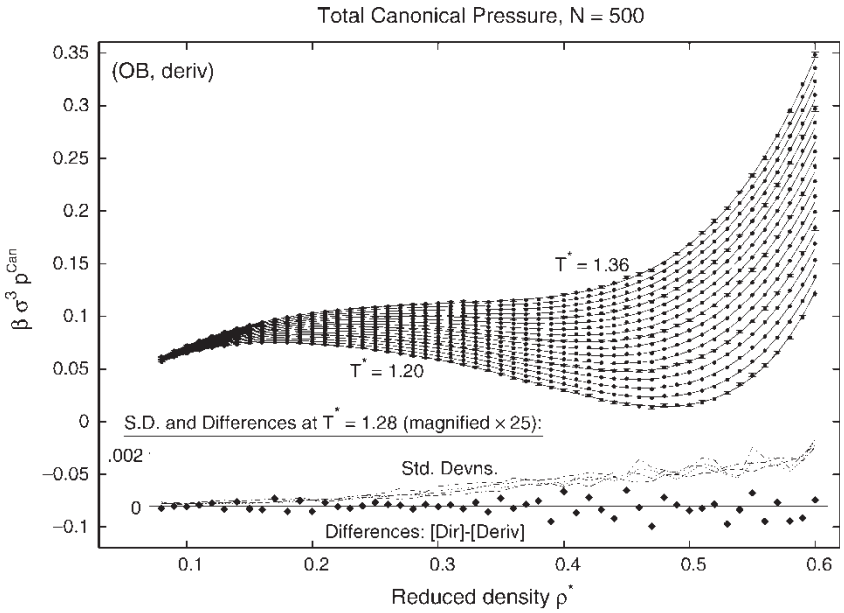

Figure 10. Pressures throughout the target region obtained in the OB investigation using the "derivative" method, shown as points, with errorbars along five of the isotherms. The solid curves are those for pressures derived from the "A-fit" to the free energy. In the inset are shown, on a scale magnified by 25, the difference between the results obtained using the "direct" and "derivative" routes to these pressures, along with the apparent standard deviations from both methods and from both the OB and 3S investigations; at $T^* = 1.28$.

various approaches. The points in the inset give the differences between the "direct" and "derivative" results, and show these to be rather random and mostly small compared to the standard deviation of each; on the other hand, these differences are no longer quite negligible compared with the standard deviations, as they are for the energy.

The differences between pressure estimates from the OB and 3S investigations (not shown) again display no systematic trend, and the range of these differences is adequately described by calculating their uncertainties from those of the separate estimates. There is a substantial number-dependence to the pressure, especially in the coexistence region: figure 11 shows this for pressure isotherms at three temperatures ($T* = 1.20$, 1.30 and 1.36). The accompanying curves are those derived by differentiating the algebraic fit to the free energy A-fit, and we see again that they are giving a faithful representation of the pressure. We can see a "flattening" of the Van der Waal's loop as the system size increases;

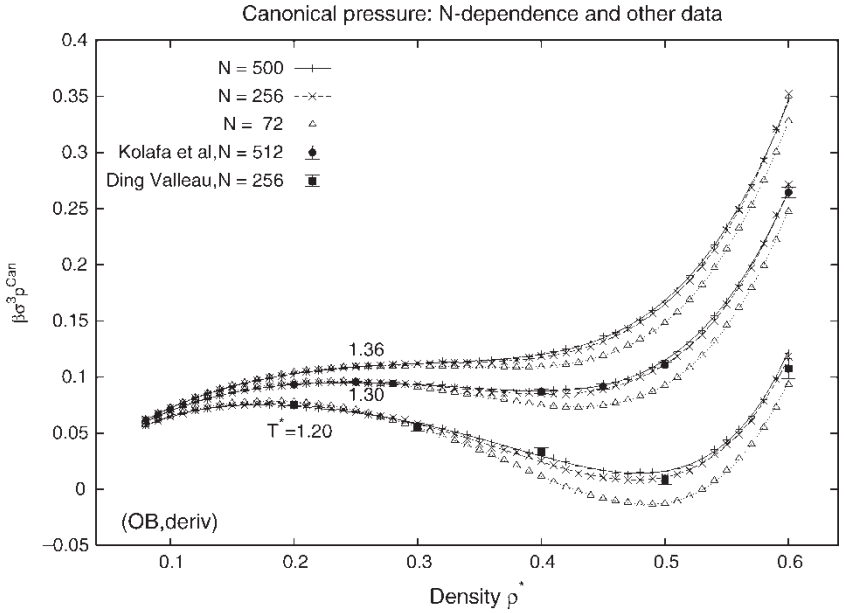

Figure 11. Size-dependence of the mean pressures along three isotherms. The points come from numerical derivatives of the (OB) free energy data, the curves are derived from the "A-fit" to the free energy. Some earlier good Monte Carlo data is also shown.

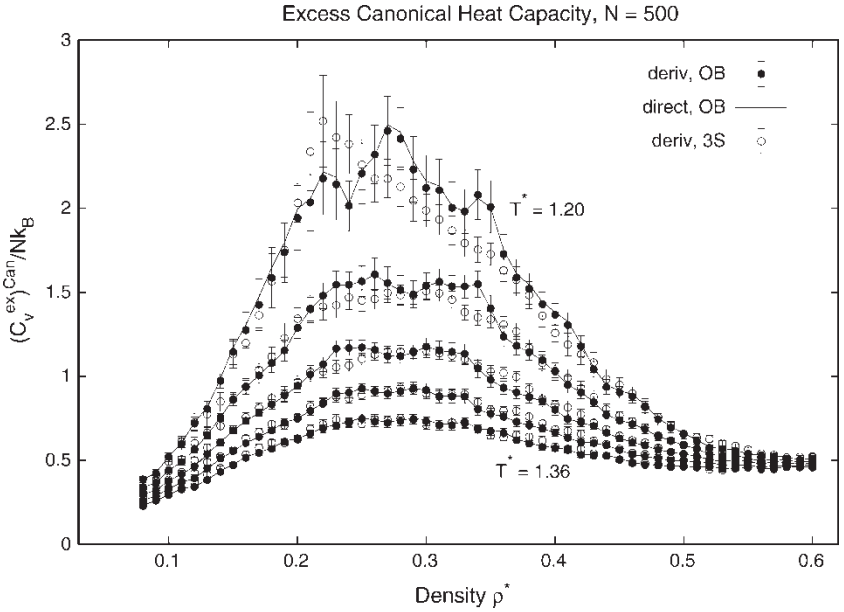

Figure 12. Estimated heat capacities along five equally-spaced isotherms. For the OB investigation, the figure shows values obtained by the "derivative" method (black circles) and by the "direct" method of averaging energy fluctuations (lines joining adjacent states); they agree well. The estimates are not surprisingly rather noisy inside the unstable coexistence region, especially at the lowest temperature. Results from the 3S investigation (open circles) are also shown.

(this involves a decrease of pressure on the low-density side of the loop and an increase on the other, but these effects are partly confused by the simultaneous effects of the temperature-shift of the whole coexistence loop as the size changes, a subject discussed below).

The intermediate temperature of $T* = 1.30$ in the figure was chosen to allow further comparison with the highly-accurate results of Kolafa et al [29]; the agreement is clearly good. The standard errors of the results of Kolafa *et al.* along this pressure isotherm are only 1.5–2 times as great as those in this TDSMC investigation. "[A]bout 40 million" Monte-Carlo steps were required to obtain the pressures and energies in these 7 states on the single $T* = 1.30$ isotherm [29] (so that to obtain precision similar to the TDSMC results would have required well over 100 million); to obtain essentially the *complete* thermodynamics, including highly accurate free energies, for 901 states along seventeen isotherms in the TDSMC investigation we used 720 million such configurations. Also shown are some earlier results for $N = 256$ at $T* = 1.20$, with errors more typical of respectable single-state simulations [30].

4.2 Second-order thermodynamic functions

The reduced canonical isochoric specific heat, C_v^{Can}/Nk, can be written as the canonical average of the fluctuations of the energy,[†] and thus estimated "directly" using equation (8). One alternative way to estimate it is to calculate (first and second) numerical derivatives of our reduced free energies with respect to the temperature—i.e. by the "derivative" method—by noting that

$$\frac{C_\nu^{\mathrm{Can}}}{Nk} = 1.5 - 2T* \left(\frac{\partial}{\partial T*} \Delta \left(\frac{\beta A^{\mathrm{ex}}}{N} \right)^{\mathrm{Can}} \right)_{\rho*} - (T*)^2 \left(\frac{\partial^2}{\partial (T*)^2} \Delta \left(\frac{\beta A^{\mathrm{ex}}}{N} \right)^{\mathrm{Can}} \right)_{\rho*} . \quad (19)$$

In figure 12 both estimates of the "excess" part of the heat capacity are shown, for five of the seventeen isotherms in the OB investigation for $N = 500$: the "derivative" results as filled circles with (one standard deviation) errorbars and the "direct" as straight-line segments joining adjacent values. The uncertainty in second-order quantities such as the heat capacity is of course much larger than that of the first-order functions, since they depend on estimating a fluctuation quantity or alternatively on taking a numerical second derivative of inherently noisy data. (The uncertainties are noticeably large at the lowest temperature, $T* = 1.20$; this is in part due to the necessary use of an asymmetrical ("one-sided") numerical estimate [28] of the temperature derivatives along this boundary of the target region.) It is clear that once more the "direct" and "derivative" estimates disagree everywhere by far less than the random errors, so they are

[†]The relationship of second-order thermodynamic quantities to the fluctuations of first order quantities is reviewed in any standard textbook, of statistical mechanics. Specific relations appropriate to the canonical ensemble, and suited to simulations of the Lennard-Jones model, may be found in ref. [7]

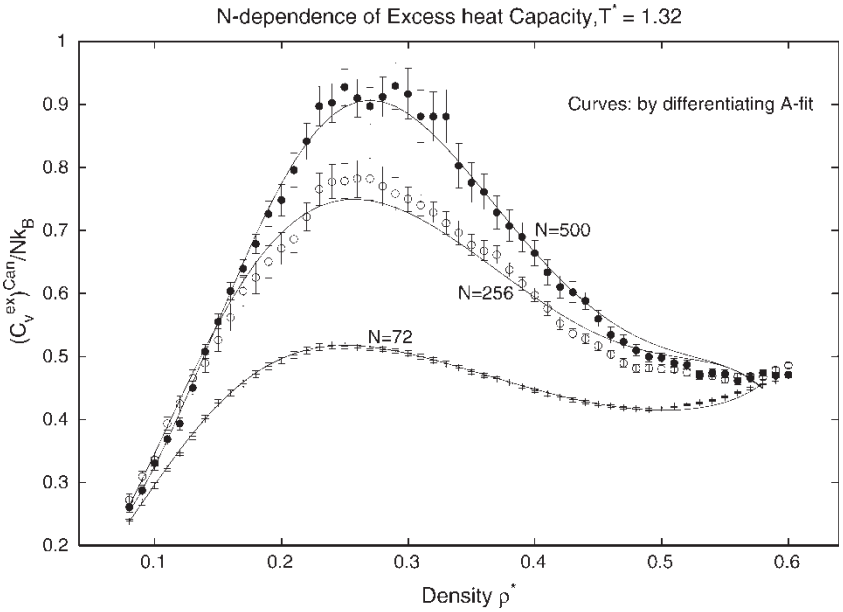

Figure 13. Heat capacities for various system sizes N, at $T^* = 1.32$.

equally satisfactory routes. The figure also shows results from the 3S study (open circles with errorbars): the two sets of results have statistical errors of similar magnitude, and the differences between them are essentially consistent with these statistical errors. It is evident that the heat capacity as a function of density tends to peak, roughly in the region $\rho* \sim 0.3$. This behaviour is to be expected near the gas–liquid transition, with the peak density slightly shifted from the critical value.

The heat capacity in this peak region is very highly dependent on the system size, which is also to be expected in view of the expected divergence at the critical point in the thermodynamic limit. This is showed in figure 13, for the temperature $T* = 1.32$, which is slightly above the expected bulk critical temperature. Figure 13 also shows the corresponding heat capacities as calculated by evaluating appropriate derivatives of the algebraic fit to the free energy previously described, the "A-fit". Over most of the range this algebraic result is very satisfactory. However, it is not entirely adequate at high densities. It should be remembered that the fit was purely to the *free energy* results, for which it was very good; no requirement that it represent the other thermodynamic properties was incorporated. However, it is possible to achieve very good agreement with the free energy itself without very close control of its temperature and density derivatives, especially the higher derivatives and especially near the boundaries of the fitted region. Although the first-order quantities remained in fact very well described by the A-fit, as we saw, the heat capacity, depending on the curvature, is less well reproduced; this suggests that the fit is doing some violence to the second derivatives near the boundaries of the fitted region. This is even more true at the boundaries corresponding to the extreme low and high temperatures of the target region; at the low temperature limit the fit even becomes qualitatively unsatisfactory. (This problem is confounded by the fact that the desired property (19) actually takes the form of a small difference between the second-derivative term and the lower-order term, thus multiplying the effect of an error in the second derivative by a factor of about five.) Therefore to represent all the properties accurately, including those of second-order, even at the borders of the target region, evidently would require a more sophisticated fitting procedure then was used for the "A-fit".

In the canonical ensemble, it is more convenient to estimate not the isothermal compressibility but its inverse, $(\kappa_T^{\mathrm{Can}})^{-1} \equiv -V(\partial p^{\mathrm{Can}}/\partial V)_T$. Once again, this can be estimated "directly" by evaluating the pressure fluctuations[†] using equation (8), or by differentiating the free energy estimates. In the latter, the "derivative", method, it is only necessary to apply the thermodynamic relation

$$\beta\sigma^3\kappa_T^{-1} = -2\beta\sigma^3 p - (\rho*)^2\left(\frac{\partial^2}{\partial\rho^{*2}}\left(\frac{\beta A}{N}\right)\right)_T, \qquad (20)$$

and recall the "derivative" expression equation (18) for the reduced canonical pressure. Once again the two methods give the same results to well within the estimated errors of either. The inverse compressibility results for $N = 500$ for two temperatures ($T* = 1.20$ and 1.36) are shown in figure 14, both for the OB investigation (as points with errorbars) and the 3S investigation (as line segments joining adjacent values); the agreement of the two sets of results is consistent with the error estimates, but these are themselves not small at the higher densities, as discussed previously. It is evident that at the lower temperature the compressibility has a negative region, corresponding to the mechanically unstable region within a first-order coexistence region.

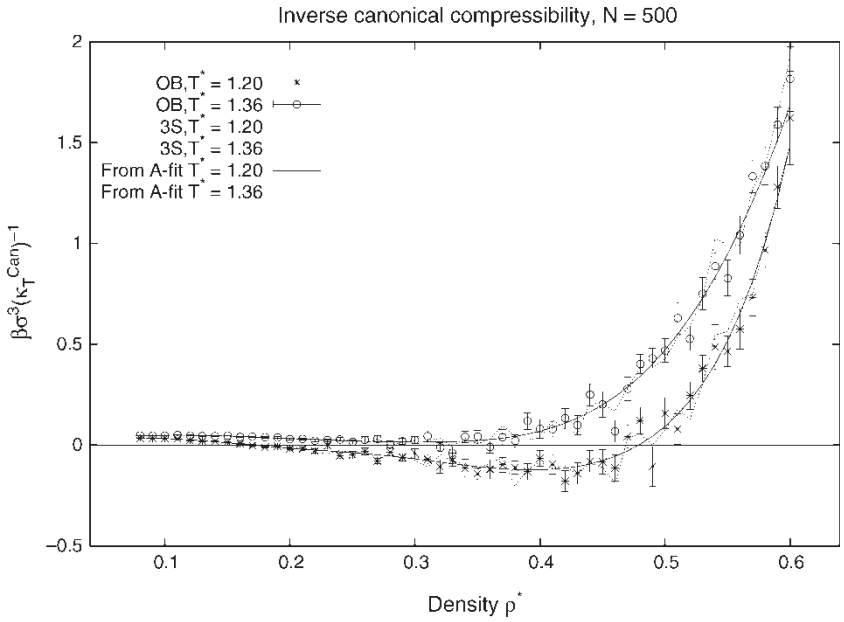

Figure 14. The inverse of the isothermal compressibility, along two isotherms. The figure shows results from the OB investigation (points with errorbars), the 3S investigation (dotted lines joining adjacent states) and derived from the A-fit (solid curves).

The figure shows also (solid curves) the corresponding results obtained by algebraic differentiation of the free-energy fit (the "A-fit"). It appears to be pretty good (and better than for the heat capacity). This is examined more closely, at a single temperature ($T* = 1.28$), in figure 15, which also displays the discrepancy between the OB and 3S estimates; they may be compared with (plus and minus) the estimated uncertainty of the OB−3S discrepancy. We see again that the OB/3S discrepancy is consistent with its error estimates, and also that the results obtained by differentiation of the algebraic "A-fit" to the estimated free energy are satisfactory (except possibly just at the upper density boundary, for reasons mentioned before). This means that the "fit" results form a useful "smoothed" version of the inverse compressibility results, easier to survey than the raw results. In figure 16, these fits are shown for $N = 500$ and for $N = 72$, at intervals of 0.04 in reduced temperature; the results for $N = 256$ lie between, and have been omitted merely for clarity. The zeros of these curves represent evidently the limits of the region of *mechanical* instability in the phase transition, i.e. points on the liquid−gas "spinodal" curve. One can see that the finite-

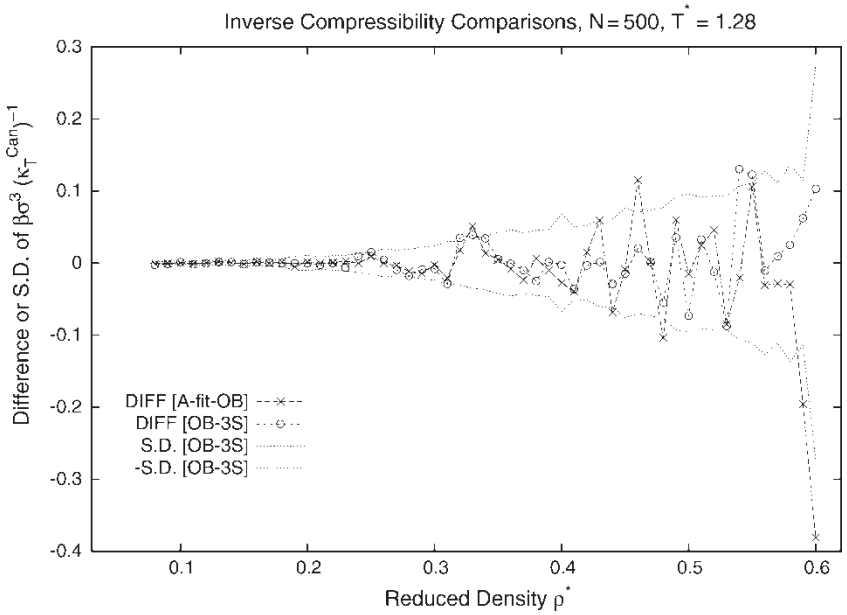

Figure 15. Inverse compressibility: differences of the 3S results from the OB, along the $T^* = 1.28$ isotherm, and also of those derived from the "A-fit". The solid curves show (plus and minus) the apparent standard deviations of the former.

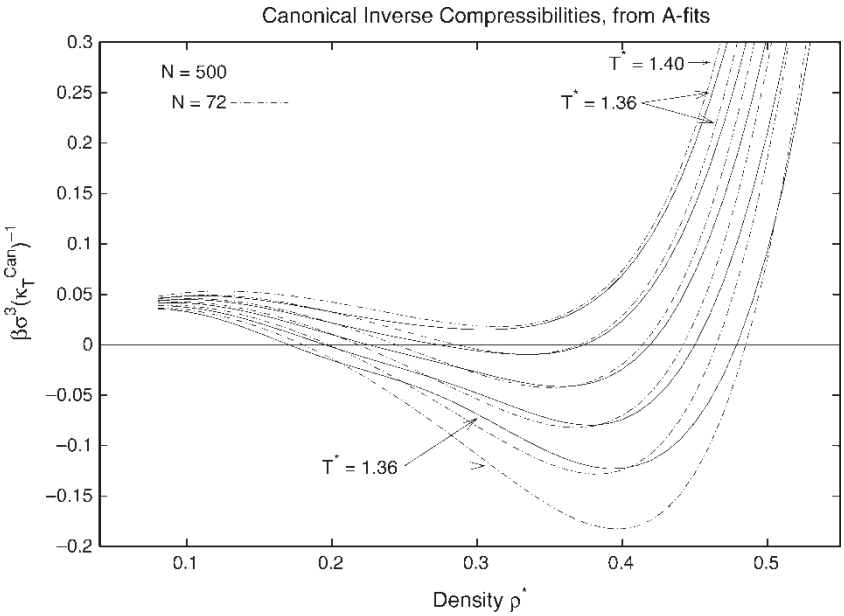

Figure 16. Fitted inverse compressibilities along various isotherms, for $N = 500$ and 72.

system critical point of the $N = 500$ system must lie somewhat below $T* = 1.34$ and that of the $N = 72$ about 0.04 higher: this is confirmed in the following section.

According to the generalised "thermodynamic" equation of state the pressure can be written as the sum $p = p_{\rm kin} + p_{\rm int}$ of the "kinetic pressure" $p_{\rm kin} = T(\partial p/\partial T)_V$ and the "internal pressure" $p_{\rm int} = -(\partial U/\partial V)_T$; these complete the basic second-order thermodynamics. In particular, the internal pressure can be expressed in terms of the correlation of the fluctuations of the energy and the pressure (or, more accurately, of energy and the virial of forces)—[†] and can thus be calculated "directly", using equation (8). Alternatively, it can be written in terms of the mixed second derivative of the free energy with respect to temperature and density, explicitly as

$$\beta\sigma^3 p_{\rm int}^{\rm Can} = T*(\rho*)^2 \times \left(\frac{\partial}{\partial T*} \left(\frac{\partial}{\partial \rho*} \Delta \left(\frac{\beta A^{\rm Can}}{N} \right) \right)_{T*} \right)_{\rho*}, \qquad (21)$$

and thus calculated from the free energies (i.e. in the "derivative" method). As usual, the two methods of estimation are in good agreement, and the differences between the results of the OB and 3S investigations are consistent with their apparent uncertainties.

Figure 17 shows the internal pressure (deriv, OB), along with the corresponding kinetic pressure and the total pressure, at $T* = 1.28$ for $N = 500$. The errors in estimating the internal pressure are surprisingly small for a second-order quantity—typically about 1%; those of the kinetic pressure are similar, since the errors in the total pressure are much smaller, as we saw. The two components of the pressure are each strikingly larger in magnitude than their sum, the total pressure. The kinetic pressure depends very weakly on the temperature, so this figure looks qualitatively much the same for all temperatures within the range studied. The curves which accompany $\beta\sigma^3 p^{\rm Can}$ and $\beta\sigma^3 p_{\rm int}^{\rm Can}$ are those derived algebraically from the "A-fit" to the free energy: the resulting description of the internal pressure is very satisfactory.

4.3 Some further thermodynamic functions

Various combinations of the above thermodynamic functions are of interest in thermodynamic discussion, e.g. the entropy and the chemical potential. We display some of their behaviour here.

The reduced specific entropy can be expressed as $S/Nk = \beta E/N - \beta A/N$. By combining the TDSMC data on reduced canonical free energies (relative to that of a reference state) with those on the internal energies (and with that of the reference state) we obtain the variation of the *relative* canonical entropy with temperature and density throughout the target region. Such results are shown (along five of the seventeen isotherms along which data were collected) in figure 18. Since the energies are extremely precise, as we saw, the expected error in these entropies is small: the standard deviation is typically between 0.002 and 0.004, rising to over 0.005 only at the lowest temperature and within the unstable density region. (In a similar way the enthalpy can of course be obtained by combining the internal energy and the pressure results).

Of more interest, perhaps, is the reduced chemical potential, $\beta\mu^{\rm Can} = \beta G^{\rm Can}/N = \beta A^{\rm Can}/N + \beta p^{\rm Can}/\rho$; we obtain its value, relative to the reference state, by combining our free energy and pressure data. Figure 19

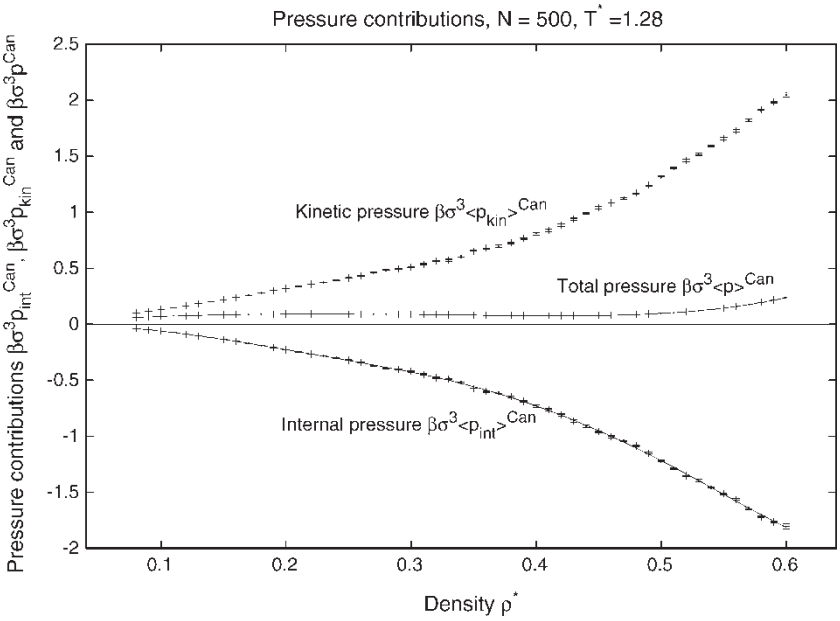

Figure 17. Estimated internal pressures p_i and kinetic pressures at $T^* = 1.28$, along with their sum, the total pressure p. The curves are results derived from "A-fit".

shows the reduced chemical potential, relative to that of the reference state at $T* = 1.20$, $\rho* = 0.08$, at all 901 states, as determined in the OB study, using the "derivative" method to obtain the pressures. The Van der Waal's loop characteristic of the first-order phase transition is evident at the lower temperatures. Along five of the isotherms are shown the estimated standard deviations and also (as solid curves) the chemical potential result derived from the "A-fit"; we see once again that the "A-fit" gives an extremely satisfactory smoothed representation of the derived thermodynamics of the system.

It is rather more fun to plot the chemical potential as a function of the pressure, instead of the density, as shown for five of the isotherms in figure 20. In this representation, the Van der Waal's loops become *closed* loops in each isotherm. The coexistence pressures and chemical potentials correspond to the coordinates of the self-intersections; the coexisting densities are given by the slopes of the two branches at the intersection (and the spinodal points by the sharp extremities of the loops, of course). The loop decreases in size as the temperature increases, finally disappearing at the canonical (finite-system) critical temperature.

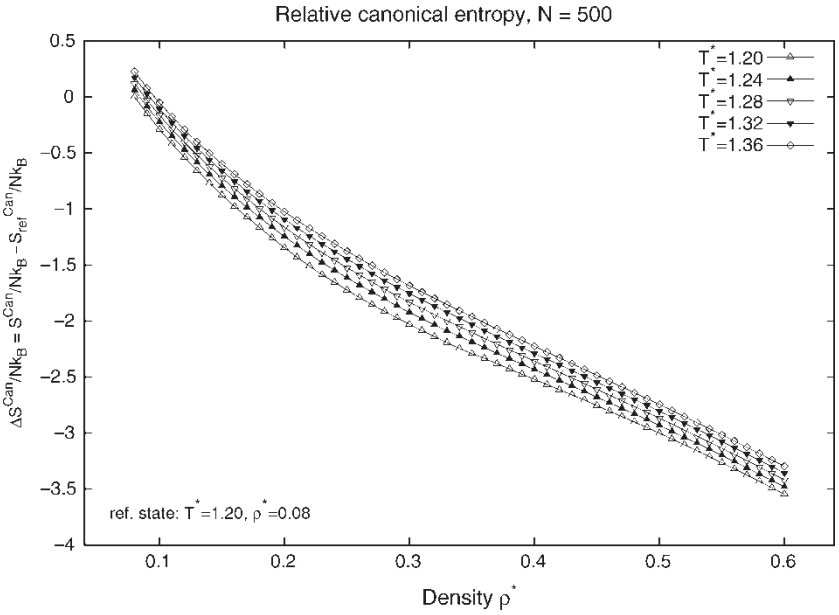

Figure 18. Relative entropy along five isotherms, $N = 500$ in the OB investigation.

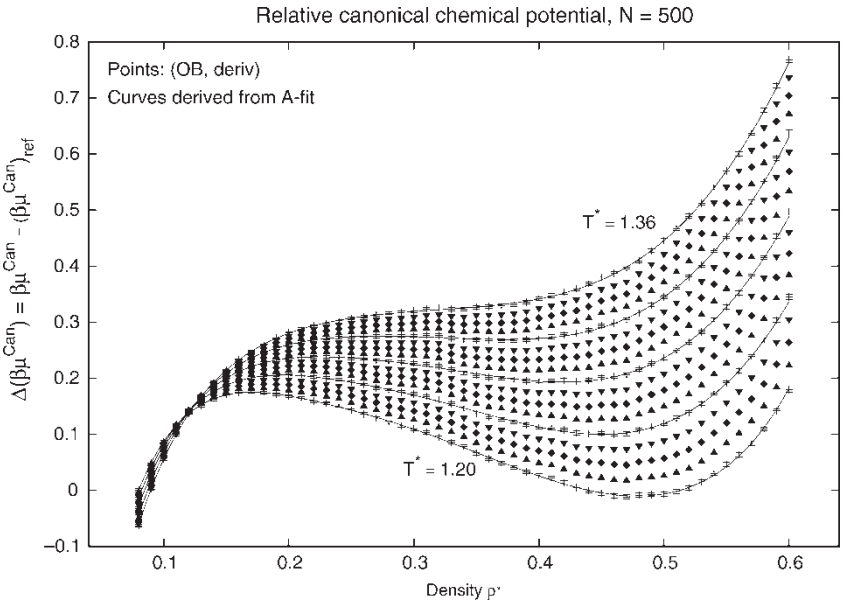

Figure 19. Relative reduced chemical potential for 901 states as a function of density along 17 equally-spaced isotherms, from the OB investigation. Error bars are given along five of the isotherms; the accompanying curves on these isotherms show the values following from the "A-fit" to the relative Helmholtz free energy.

5. Liquid–gas coexistence

The target region of temperature and density in the study was chosen to include the upper part of the liquid–gas coexistence curve of the Lennard-Jones model under study. Indeed we have seen evidence of that in the Van der Waal's loops of the chemical potential and the pressure, the peaks in the heat capacities, the sign changes in the compressibility, and in particular in the appearance of concave portions in the free-energy isotherms when plotted as a function of volume (cf. figure 4). In order to locate the coexistence data for the model we in fact used the "double-tangent construction" on those free-energy isotherms, noting that the double-tangent to such a free energy isotherm has a slope which is minus the vapour pressure, and that the tangent points occur at the densities of the coexisting phases; an example is shown in figure 21.

Of course, the raw free energy data was collected only at discrete reduced densities, at intervals of 0.01. To estimate the coexistence data as precisely as possible, it is convenient to interpolate the free energy locally, in the vicinity of each double-tangent point on every subcritical

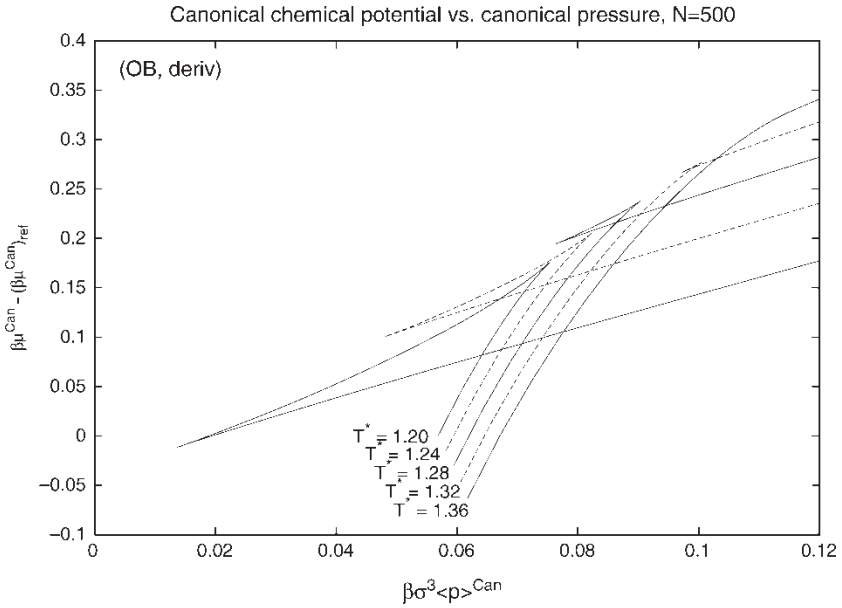

Figure 20. The chemical potentials as a function of the estimated pressure, along five of the isotherms (plotted as straight-line segments joining adjacent points along each isotherm). The coexistence pressure and chemical potential are given by the self-intersections, and the (inverse) densities of the coexisting phases by the two slopes at these points.

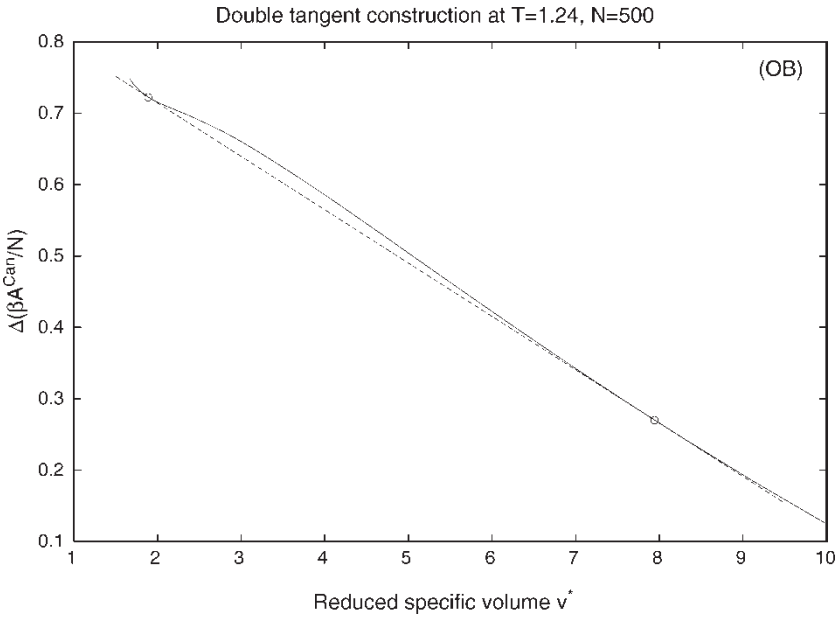

Figure 21. Illustration of the "double tangent" construction to the free energy, at a subcritical temperature $T^* = 1.24$. The details of the procedure used to locate the tangent are described in the text. The dashed line is the estimated double tangent (the slope of which gives the vapour pressure), and the open circles mark the tangent points, which lie at the specific volumes and free energies of the two coexisting phases.

isotherm studied. This was done by making an (unweighted) least squares fit, to a quadratic in the specific volume, of the five data points closest to each double tangent point. It is then easy to locate the common tangent to these local fits, and hence to find the coexisting densities and the vapour pressure with some precision. The statistical error in these estimates can be estimated from (i) the standard uncertainty in the parameters of the two local fits, along with (ii) the standard error of the free energy difference of the two coexisting phases (closely approximated by that between the nearest raw data points). In practice, we considered all possible combinations of plus and minus these standard deviations, treated as independent, and for each property chose the *worst case* among them to give our estimate of probable error. (Due to the substantial covariances between the fitting parameters, this worst case should considerably overestimate the errors, in principle. On the other hand, the estimates of the standard deviations of the fitting parameters will not themselves be highly accurate in view of the small number of data points involved in their estimation.) These data are summarised for $N = 500$ (for the OB study) in table 3.

Figure 22 shows the coexisting densities at various temperatures for $N = 72$, 256 and 500 (all from the OB study). At the lower temperatures the uncertainties of the coexisting densities are extremely small; naturally these uncertainties increase as one approaches the critical region, however, due to enhanced difficulty in specifying the double tangent points given the very small curvatures in the free-energy/volume curve in that region. Of course, it is also possible to derive the coexistence curve corresponding to the global algebraic "A-fit" to the free energy discussed previously. The resulting coexistence curves and rectilinear diameters are shown (as solid curves) in the figure. The fit appears to give a very faithful reproduction of the location of the coexistence densities as determined above, except that it deteriorates

Table 3. Canonical coexistence data, $N = 500$.

T^*	$\rho_g^* \pm$ sd	$\rho_l^* \pm$ sd	$\beta\sigma^3 p_{vap} \pm sd$
1.200	0.09824 ± 0.00033	0.56791 ± 0.00059	0.06414 ± 0.00007
1.210	0.10434 ± 0.00043	0.55822 ± 0.00051	0.06672 ± 0.00008
1.220	0.11092 ± 0.00043	0.54825 ± 0.00036	0.06936 ± 0.00007
1.230	0.11814 ± 0.00045	0.53833 ± 0.00022	0.07205 ± 0.00008
1.240	0.12591 ± 0.00041	0.52823 ± 0.00056	0.07481 ± 0.00009
1.250	0.13452 ± 0.00050	0.51737 ± 0.00099	0.07766 ± 0.00009
1.260	0.14375 ± 0.00057	0.50580 ± 0.00140	0.08056 ± 0.00010
1.270	0.15391 ± 0.00087	0.49224 ± 0.00070	0.08351 ± 0.00011
1.280	0.16560 ± 0.00114	0.47979 ± 0.00067	0.08653 ± 0.00012
1.290	0.17908 ± 0.00129	0.46528 ± 0.00322	0.08968 ± 0.00014
1.300	0.19365 ± 0.00177	0.44409 ± 0.00285	0.09285 ± 0.00015
1.310	0.21149 ± 0.00293	0.42375 ± 0.00445	0.09608 ± 0.00018
1.320	0.23966 ± 0.01040	0.40156 ± 0.00212	0.09939 ± 0.00022

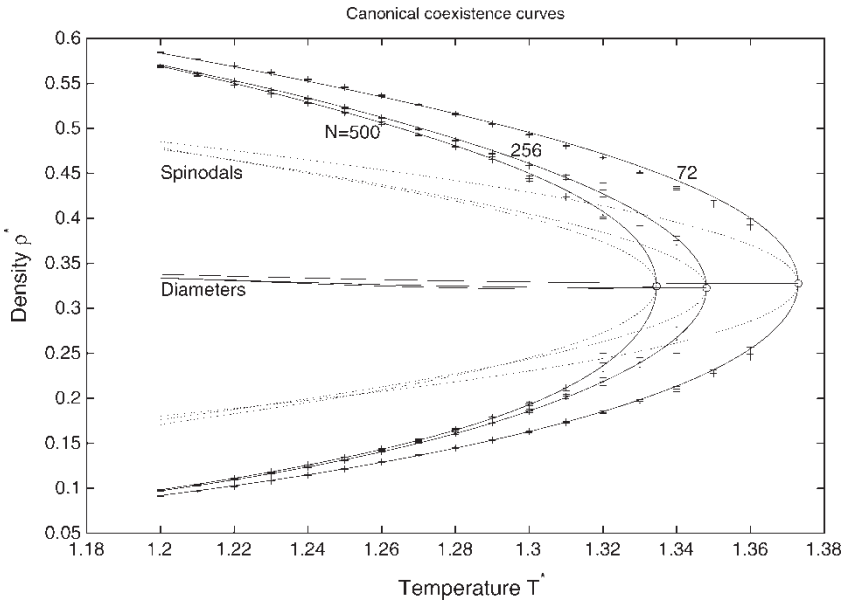

Figure 22. Derived canonical coexistence curves for systems of various sizes. The points with errorbars are from direct numerical analysis of local free energies at each temperature. The curves are those predicted by the "A-fit" for each size: as well as the resulting densities of the coexisting phases (solid curves), the figure shows the predicted rectilinear diameter (also solid), spinodal curves (dotted) and critical points (open circles). The shift of the finite-system canonical critical temperature as the system size changes is striking but expected.

somewhat as the critical region is approached (especially in the case of the small ($N = 72$) system). (This deterioration is not surprising, and is again connected with the small curvatures in the free-energy/volume behaviour: the curvatures of the "A-fit" need not be highly accurate even though the free energy itself is fitted very accurately. A more sophisticated fitting procedure might avoid this difficulty.) As usual, the 3S study led to results similar to the OB results reported.

The "A-fit" to the free energy embraces the finite-system critical region, evidently, and so allows us in principle to derive the *whole* of the coexistence curve, and thus to extract estimates of the critical temperature and density (and pressure) for these finite systems (in the canonical description). These are shown (open circles) on figure 22. (For $N = 500$ the resulting apparent canonical ensemble finite-system critical temperature and density turn out to be $T* = 1.3345$ and $\rho* = 0.324$; the likely precision of these estimates of the location of the critical point is discussed below.) We see the expected very strong size dependence of the location of the finite-system canonical coexistence curve and critical point. The figure also shows the rectilinear diameters, along with (as dotted curves) the spinodal curves (obtained by seeking the maximum and minimum of the pressure (as derived from the "A-fit") along isotherms within the coexistence envelope).

Figure 23 shows the corresponding vapour pressure data. Of particular interest is the tiny uncertainty in the vapour pressures, in the range from 0.1 to 0.2%. This results from the fact that the vapour pressure is obtained here as the slope of the double tangent, and its uncertainty therefore depends primarily on the uncertainty (very small as we noted) in the relatively large difference between the free energies of the coexisting phases, directly evaluated from the TDSMC results (cf. Appendix B). (By contrast, it is usually necessary, when using more conventional ways of studying the coexistence, to make direct *local* estimates of the pressure of each of the coexisting phases, with the usual large fuctuations and substantial statistical error.) It is also easy to understand why the precision of our *vapour pressure* estimation deteriorates much less noticeably than that of the coexistence *densities* as the temperature rises toward criticality, since while the uncertainties of these densities increases, the sensitivity of the vapour pressure to those uncertainties is simultaneously decreased, due to the decreasing curvature of the free energy. The dashed curves are vapour pressures as derived from the fits "A-fit" (to which the same remark about precision applies). The corresponding predicted critical point for each N is shown as an open circle.

Table 4 compares these coexistence results (for $N = 500$ at a few temperatures) with some published estimates. In some cases they are not strictly comparable, having been determined using data from ensembles other than the canonical and/or employing data for systems of varying size. Nevertheless, they practically all agree with the TDSMC values within their own (mostly rather large) uncertainties; on the other hand they mostly disagree by far more than the much smaller estimated uncertainties of the present values. What is perhaps most interesting to see in this table is the very rapid improvement in precision over the last several years. The estimates of Mecke *et al.* [27] and of Lotfi *et al.* [31] appear to be of remarkable quality (although the expected errors of the former are uncertain, and those of the latter still rather large compared to those of the present study), while the recent results of Errington [34] appear so precise that the discrepancy from the present canonical-ensemble results

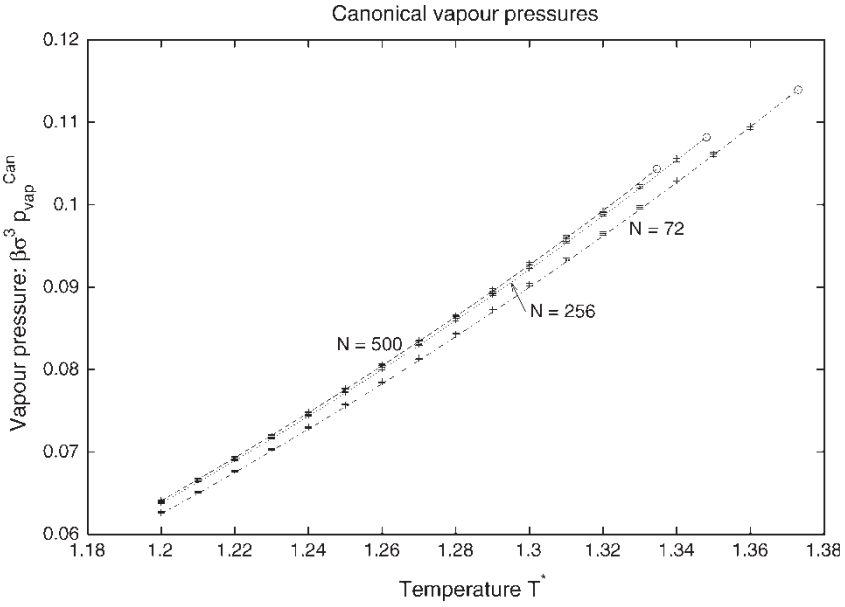

Figure 23. Estimated vapour pressures. The points with error bars come from direct analysis of the original free energy data. The curves are the predictions from analysis of the algebraic "A-fit" of the free energies, terminating in the predicted critical points (open circles).

may largely be due to their belonging rather to the isothermal-isobaric ensemble.

It is easy to derive the remaining canonical thermodynamics of the vaporisation. The difference of Helmholtz free energy of the coexisting phases is already implicit in the estimation of the vapour pressure, as mentioned; in order to find the internal energy difference the energy data for gas and liquid were interpolated to their coexistence values using a quadratic fit to the five neighbouring raw data points. Combining such results leads (for $N = 500$) to

Table 4. Comparisons with some published coexistence data.[‡]

Source	*Method*	*Gas density* $\rho_g^* \pm$ sd	*Liquid density* $\rho_l^* \pm$ sd	*Vapour pressure* $p_{vap}\sigma^3/\epsilon \pm$ sd
		$T^* = 1.30$		
Present work	TDSMC,Can'l	0.1937 ± .0018	0.4441 ± .0029	0.12070 ± .00020
Mecke *et al.* [27]	EOS	0.1891 ± −	0.4514 ± −	0.12016 ± −
Lotfi *et al.* [31]	(*N*,*p*,*T*)	0.195 ± .011	0.428 ± .015	0.1204 ± .0023
Johnson *et al.* [26]	EOS	0.220 ± −	0.410 ± −	0.1229 ± −
Smit and Frenkel [32]	GEMC	0.20 ± .05	0.42 ± .07	0.121 ± .008
				0.118 ± .007
Panagiotopoulos *et al.* [34]	GEMC	0.21 ± .01	0.46 ± .03	0.121 ± .006
				0.126 ± .012
Panagiotopoulos *et al.* [33]	GEMC	0.24 ± .02	0.45 ± .03	0.125 ± .007
				0.114 ± .007
Adams [35]	GCMC	0.22 ± −	0.43 ±	0.127 ± −
		$T^* = 1.25$		
Present work	TDMC,Can'l	0.13452 ± .00050	0.51737 ± .00099	0.09707 ± .00012
Errington [36]	(*N*,*p*,*T*)	0.1383 ± .0016	.5076 ± .0020	.09733 ± .00030
Mecke *et al.* [27]	EOS	.1330 ± −	.5145 ± −	.09684 ± −
Lotfi *et al.* [31]	(*N*,*p*,*T*)	.1339 ± .0067	.5125 ± .0026	.0973 ± .0011
Johnson('93) et al [26]	EOS	.1394 ± −	.5118 ± −	.0986 ± −
Panagiotopoulos [34]	GEMC	.152 ± .015	.529 ± .009	.101 ± .009
				.102 ± .016
Panagiotopoulos [33]	GEMC	.123 ± .014	.505 ± .023	.091 ± .009
				.091 ± .014
Adams [35]	GCMC	.19 ± −	.544 ± −	.111 ± −
		$T^* = 1.20$		
Present work	TDSMC,Can'l	.09824 ± .00033	.56791 ± .00059	.07697 ± .00008
Errington [36]	(*N*,*p*,*T*)	.0993 ± .0005	.5657 ± .0019	.07705 ± .00018
Mecke *et al.* [27]	EOS	.0983 ± −	.5658 ± −	.07694 ± −
Lotfi *et al.* [31]	(*N*,*p*,*T*)	.0987 ± .0016	.5661 ± .0022	.07718 ± .00066
Johnson *et al.* [26]	EOS	.1005 ± −	.5669 ± −	.0781 ± −
Smit and Frenkel [32]	GEMC	.098 ± .010	.564 ± .016	.076 ± .004
				.08 ± .02

[‡] The figures in Table 4 were kindly communicated by Prof. Errington.

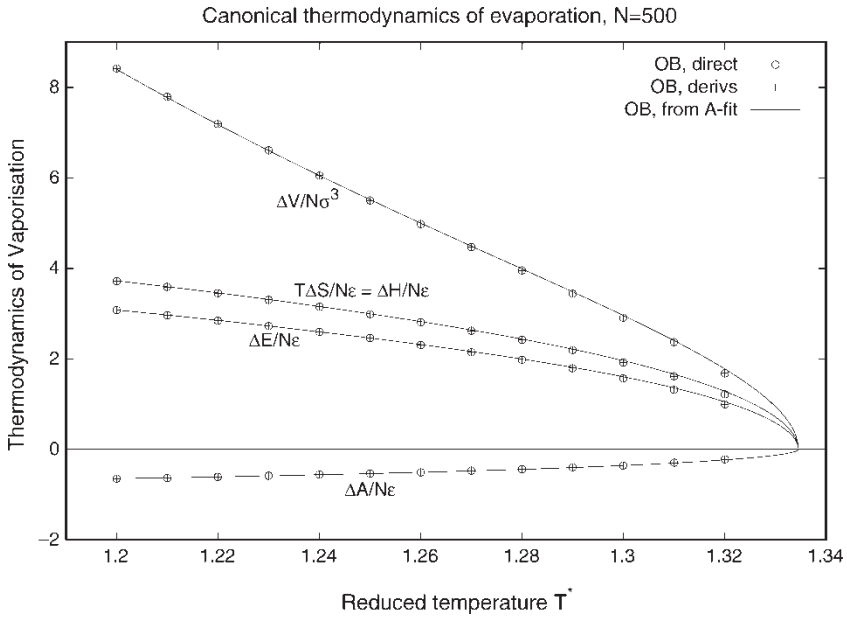

Figure 24. Apparent thermodynamics of the evaporation of Lennard-Jonesium. (Note that the thermodynamic quantities are here all "reduced" using the Lennard-Jones parameters.) The data points confirm that there is no visible discrepancy between using "direct" and "derivative" methods of obtaining these quantities; the curves show the predictions derived from the "A-fit".

the points shown in figure 24, which are for the OB investigation. In each case these results are given based on determining the first-order thermodynamic quantities both by "direct" averaging (open circles) and by taking "derivatives" of the free energy (+ symbols): the fact that they appear to coincide reflects again the equivalence of these two approaches to extracting the results. It is also easy to generate such estimates of the thermodynamics of vaporisation from the algebraic free-energy fit "A-fit" and such results are shown as curves in the figure. The accuracy of these numbers derived from the A-fit is excellent, but it does deteriorate somewhat as one approaches close to the critical region, for the reasons already discussed.

We have noted the decreasing precision of the "A-fit" estimates of the thermodynamics of coexistence, as criticality is approached, and explained why it may be expected (at least with the simple fitting procedure used). It is, of course, frustrating, and especially so because these fits represent the route to locating the (finite-system) critical points (e.g. those shown on the above figures). Some uncertainty is, of course, inherent in any determination of the critical point by what is basically an extrapolation procedure, but one might hope to have reduced this problem significantly by use of a global fitting procedure (to rather precise data) such as that of "A-fit"; this is only partially the case, however, basically because the estimates depend sensitively on the very small *curvatures* in the fitted free energy, as mentioned above. It is rather difficult to ascertain the likely resulting errors in these finite-system critical constants derived from the "A-fits". Some judgment can be made by internal analysis of the data (e.g. by carrying out the coexistence analysis independently on separate *parts* of the whole OB run) and by comparing the OB and 3S estimates; this suggests that one may perhaps not be able to count on the accuracy of T_c to better than 0.3%. For a given value of T_c the vapour pressure is very accurately determined, but the estimated 0.3% uncertainty in T_c then corresponds to a 1% doubt about p_c.

In figure 25 are plotted the apparent (finite-size) critical temperatures obtained, for the various system sizes, from the "A-fit" to the OB free-energy data, and as well those obtained from the completely independent 3S investigation (for which a slightly different fitting function, but of comparable quality, was used). The temperatures are plotted against $N^{-1/3\nu}$, where the correlation-length exponent ν was given its Ising value of 0.63. According to one surmise these canonical finite-system critical points may approach the thermodynamic limit in a way which would correspond to linearity in this graph; a linear fit to all six data points, using unweighted least squares, yields as extrapolant a proposed bulk critical temperature of 1.313 ± 0.005.

A matter of interest is the shape of the coexistence curve. The Lennard-Jones fluid is believed to belong to the Ising-like universality class, so that near the critical region the order parameter $\delta\rho \equiv (\rho_l - \rho_g)$ should behave as $(T_c - T)^\beta$ plus correction terms, with $\beta \approx 0.326$, at least in the thermodynamic limit. (This β is not to be confused with the $\beta \equiv 1/k_B T$ used elsewhere in the paper.) On the other hand a small finite system is expected to show a "crossover" to classical behaviour ($\beta \approx 0.50$) very close to the critical temperature, since the finite size will limit the range of fluctuations allowed. (And indeed, if $(\delta\rho*)^2$ is plotted as a function of the temperature $T*$ the present data appear to approach zero at the finite-system critical temperature with a finite slope; however, at lower

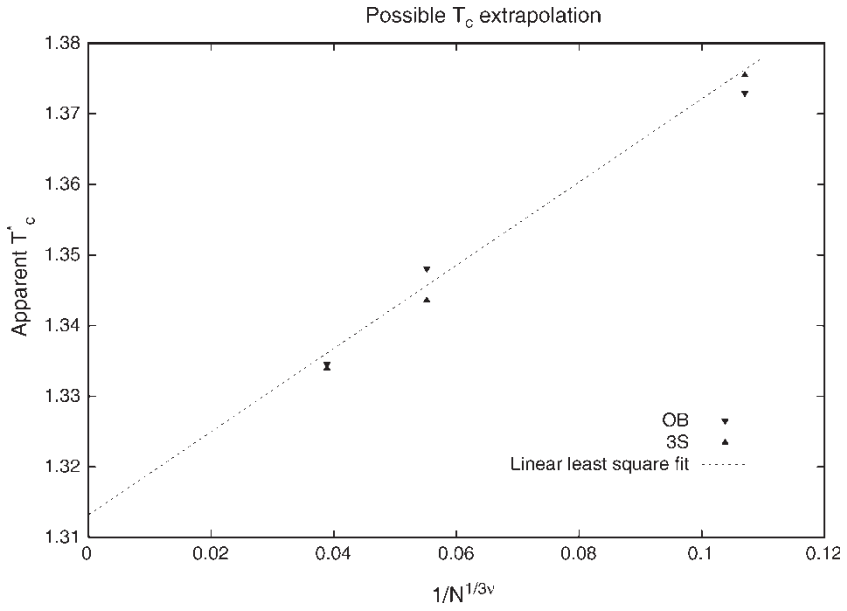

Figure 25. Apparent finite-size critical temperatures derived from algebraic free-energy fits, both for the OB investigation and the 3S, plotted as a function of $N^{(-1/3\nu)}$. The dashed line shows an unweighted linear least-squares fit of all six points.

temperatures such plots are clearly concave, indicating the expected weaker dependence on $(T_c - T)$.) It has often been thought natural to look at plots of $(\delta\rho^{\mathrm{Can}})^{1/\beta}$, with $\beta = 0.326$, which to the leading approximation would be linear for macroscopic Ising-like behaviour (with an intercept constituting an estimate of the critical temperature in the absence of a finite-size crossover). Such plots are given in figure 26 for the present (OB) data, and display both the direct determinations of the density gaps (points with errorbars) and those derived from the free energy A-fits. The results show the expected strong finite-size convexity at the higher temperatures for each N. However, considering the apparent precision of the results, it is clear that they are in fact *everywhere* substantially convex. (Indeed, it would require a β around 0.4 to straighten out the low-temperature portions of these plots—but no meaning should be attached to this number.) We were not encouraged to attempt an analysis of the discrepancy from Ising-like linearity in terms of the expected corrections to scaling: there is no clear indication of any narrow band of temperatures in which a finite-size "crossover" may be occurring (merely a gradual change of curvature with temperature), and meanwhile the large shift of the curves with system size (even well below criticality)

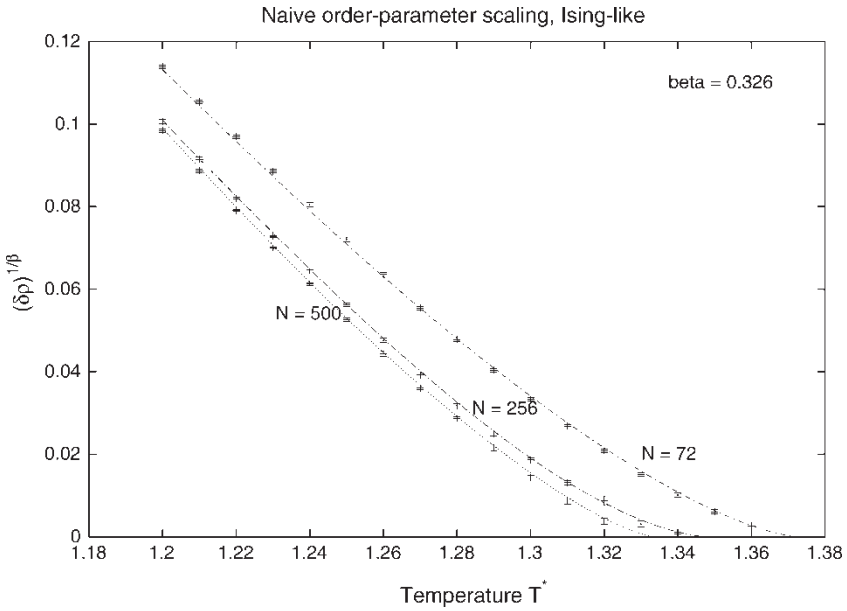

Figure 26. Finite-size scaling plot of the order-parameter $\Delta\rho$, assuming the Ising value of the critical exponent β. (At temperatures sufficiently below critical to avoid finite-size effects, such plots would be expected to be linear, except for corrections to scaling).

suggests that such naive approaches to analysing canonical coexistence data are unlikely to be reliable.

As mentioned in the Introduction, we postpone more serious attempts to analyse our present canonical data for detailed information on critical behaviour, although precise data likely to be useful in such an analysis is accessible. From TDSMC runs not reported here we also have thermodynamic data, including heat capacity and compressibility data, for a substantial supercritical temperature range and a small range of densities near the critical isochore (for $N = 72, 256, 500$ and 864, and up to at least $T* = 1.40$); their analysis could be interesting, but need not be straightforward. The formulae of finite-size scaling, as applied to lattice systems and to liquids in the grand canonical ensemble, appear inappropriate for these canonical results, which indeed show a *real* finite-size critical point (marked for example by an infinite compressibility) at a temperature quite remote from the bulk critical point: a modified form of finite-size analysis is required. A study beginning the design of such an analysis has recently been introduced by Kim and Fisher [37]; we postpone for now the attempt to examine further the present canonical data in this regard.

6. Conclusion

We have tried to exhibit the capabilities of "temperature-and-density-scaling Monte Carlo" (TDSMC) by presenting the results of such a study of the thermodynamics of a Lennard-Jones fluid over a substantial region of thermodynamic states, one including the upper portion of the liquid–gas coexistence region. The Helmholtz free energy is obtained directly, for arbitrarily-many thermodynamic states within the target region, along with the first and second order thermodynamic properties. It is also easy to derive the location and the thermodynamics of the gas–liquid coexistence. The precision of all these thermodynamic estimates turns out to be unexampled; this is particularly the case for the free energy. Furthermore, the results may be obtained in an essentially continuous way throughout the target region of thermodynamic space. The results represent a significant enhancement of our knowledge about the Lennard-Jones model (or at least of the common version of that model studied here).

The basic investigation was accomplished (for each system size N) in a *single* TDSMC run (OB), and it is these data which were reported for each property. Data were typically collected at 901 thermodynamic states in the target range ($0.08 \leq \rho* \leq 0.60, 1.20 \leq T* \leq 1.36$). In order to do this, it is necessary to choose a suitable sampling distribution π for the Monte-Carlo Markov chain, which sounds daunting: in fact this turns out to be quite straightforward in practice, and we discuss in detail one way of doing so. Except for the form of the distribution π, the Monte Carlo sampling is carried out exactly as for conventional canonical "Metropolis" applications; as discussed above, the runs are in some sense extraordinarily efficient.

The purpose of the paper is not only to report on the Lennard-Jones fluid, but also to provide a detailed outline of the methods of carrying out TDSMC studies. We also explored some possible variants in the application of the TDSMC method. For example, one's intuition might lead one to anticipate that the efficiency of the investigation could be improved by segmenting the target region into adjoining segments, each studied by its own TDSMC run, and afterward combining the results to give data over the whole region. This was examined by carrying out a complete, parallel but independent, investigation (3S), in which the target region was segmented into three regions of different density ranges. The resulting data confirm the accuracy of our results (and in fact the validity of our error estimates), but, at least for this system, there is no improvement in efficiency. This finding is perhaps surprising and it is not completely understood. Since the analysis of the results is very much more complicated for segmented samples (3S) then for one big run (OB), there is a strong indication to use the latter if this insensitivity to segmentation is confirmed in general.

Another choice concerns the estimation of first and second order thermodynamic quantities. We indicate how to estimate the corresponding quantities using *ensemble averages* collected during the run (equation (8)); this is a "direct" method. Alternatively, since estimates of relative free energy are immediately available from the run, as a function of temperature and density, the remaining thermodynamics can in principle be estimated by numerical differentiation of this quantity: the "derivative" method. To investigate this, we did the estimates *both ways*. The results agree, and it turns out also that there is no substantial difference in the corresponding error estimates, though perhaps the "derivative" method is slightly preferable in this respect. (This is rather surprising, perhaps, since the numerical differentiation of inherently noisy data is not usually an attractive prospect; the success depends on the remarkable precision of the TDSMC free energy data, which even allows useful second derivatives to be taken.) There is a strong argument for relying on the "derivative" approach, because one then need only to collect the data necessary to provide a single average for each thermodynamic state recorded (cf. equation (7)), rather than calculating and storing different rather complicated data related to each thermodynamic property of interest, a task requiring in itself computer time comparable to the generation of the Markov chain.

The outstanding precision obtained in TDSMC for the free energies of even widely separated states remains remarkable and perhaps not thoroughly understood; it is no doubt helpful that, due to the very flat sampling distribution, the "tails" of the distributions for individual states will be better sampled then in ordinary Metropolis sampling. It is easier to see that use of the required very broad sampling distribution will tend to eliminate

sampling problems of the kind referred to as "quasi-ergodic", and which are to be expected in conventional, single-state, simulations near the coexistence and critical regions. These problems are associated with the likelihood of such states involving two or more dissimilar structures, corresponding to separate regions of configuration space between which transitions are rare under conventional (fixed T and V) sampling. In TDSMC, on the other hand, one does not depend on such transitions. Instead the sampling will repeatedly be carried off to regions of the reduced space $\mathbf{r}^N$ corresponding to quite different structures, relevant to other states, to return to those of any particular state from a new direction each time. One may thus expect to sample (with appropriate relative probability) all the structures relevant to each state. And indeed we have seen no extra sampling problems for states in the metastable, unstable or critical regions of the liquid–gas coexistence: we believe the sampling is covering all the relevant configurations of each state.

The central pair forces of models like the Lennard-Jones are, of course, particularly simple to work with. Nevertheless, the techniques used here are in principle applicable to more complex particles, such as molecules. The extra complication comes from the more complicated geometry of particle interaction (as expressed using reduced coordinates), which will mean distinct calculations for each density considered (and with little help from the sort of distance-scaling which simplifies the central-force models). Such programmes will evidently run slower than those reported in this paper, but should be straightforward.

Since the states sampled are defined in terms of the values of (N,V,T), it is natural to use the results to generate thermodynamics within the canonical ensemble, as we have done above. Of course, the thermodynamics is independent of the choice of ensemble in the thermodynamic limit, but this is in principle not the case for the small systems accessible to simulation. The results of simulation tended until recently to be rather imprecise, so little attention was paid to this matter, but with the accuracy of estimation now possible it cannot be ignored. It is, therefore, appropriate to study such effects explicitly, as we do in related papers [19–21]. In addition, one wants to be able to use the results of simulation to study such subtle things as the critical behaviour of model fluids: here the choice of ensemble cannot be disregarded, because the different ensembles constrain in different ways the fluctuations on which the critical behaviour turns. For such purposes, the canonical ensemble results produced in this paper are probably not the most useful ones, in that the density fluctuations of a finite system are constrained much more severely than in the grand canonical or isothermal-isobaric choices. The "finite size scaling" procedures that have been useful in those ensembles cannot very readily be applied directly to the canonical behaviour of finite systems. For example the matching to an Ising universal shape at criticality of a mix of density and energy-density distributions, in the procedure known as "mixed-field finite-size scaling", due especially to Wilding and Bruce [see e.g. 38], is entirely impossible with canonical results. One response to this problem would be to try to develop a new form of "finite size scaling" analysis, appropriate to canonical data; a start on this has been made recently [37]. Another, in the present context, might be to ask whether we can exploit TDSMC data instead in other ensembles (for which the analysis tools are more advanced); this is a further purpose of the work we report elsewhere [19,21].

Acknowledgements

The author owes a special debt to his colleague Glenn Torrie. Many conversations with Stu Whittington and Ray Kapral have been helpful. Ian Graham kindly provided the search programme used for the non-linear "A-fit"; Professor Errington very kindly communicated some unbublished data. The work has been supported by grants from the Natural Sciences and Engineering Research Council of Canada.

Appendix A: Proposal for more economical calculation of π: "Moving Window" sampling distributions

The sampling distribution $\pi(\mathbf{r}^N)$, as computed in this paper, requires evaluating for each trial Monte-Carlo configuration the complete sum (9) of terms for *all* of the predetermined set of grid states $k \equiv (T_k, \rho_k)$ included in equation (9), distributed throughout the target region. Although this was not onerous, it is actually wasteful. The reason is that (unless N is very small) a given configuration will lead to *substantial* contributions from only a restricted set of the k-terms; the rest can safely be ignored in evaluating π for that configuration. This leads to the idea of including only an appropriate "window" of the terms in calculating the sampling weight for each configuration. Of course, one must be able to specify the size and shape of the "window"; furthermore the "window" must move around as the system's configurations change.

The economy of this is potentially very important if one wishes to study very large systems, because it is essential, if there is to be adequate sampling mobility, that the regions of configuration space associated with adjacent k-states overlap considerably. Since the relative widths of the individual k-distributions narrow as the system size N increases, one would eventually need a higher density of, and therefore (if all k were included) a higher number of, k-states, making the calculation of π more onerous. (In the present application we simply used an unnecessarily-large number of states k for all

the system sizes considered, but this means that the efficiency is not optimal.) This problem associated with increasing N is easily overcome using "moving windows", because the density of states within the window can be adjusted to suit the system size, and at the same time the breadth of the window required will correspondingly decrease as N increases. (What is needed to evaluate the part of (9) included in the window is a reasonable approximation of the excess free energy of each k-state included. These k-states need not correspond to the target states, of course, but in view of the smoothness of the excess free energy the required excess free energies can be adequately approximated by interpolation of those at the adjacent target states if necessary. (Recall that in principle the results are correct for an *arbitrary* sampling distribution π: i.e. there is no need for *exact* values, only for a well-defined π satisfying the "smoothness" criterion described in the subsection 2.2, throughout the target region of thermodynamic states.))

In principle, the appropriate window could be found empirically for each trial configuration in a direct way. One could search out, say, the state k giving the maximum contribution to π, then include in π only surrounding states k giving at least some small fraction of that contribution. We have not tried this self-monitoring.

We applied a "moving windows" approach in a TDSMC study of the Restricted Primitive Model of ionic systems [Largely unpublished, except for a few results in 39 & 40]. In this case one can expect a given configuration to contribute over only a very narrow density range. This is because in any configuration of importance there is almost certain to be a pair of ions with separation very close to the hard-core repulsive diameter; the reduced nearest-neighbour distance in the configuration then specifies this relevant density region. Extensive tests showed that (even for quite small systems) it was adequate to include *only one* density in the window, namely that corresponding to the highest density allowed by the closest ion separation in the configuration! Considerable saving of computational time resulted with no loss of precision. (We included temperatures T_k over the whole target range, however, without detailed tests of the necessity of doing so, in the expectation that each configuration will in practice contribute substantially over a considerable temperature range.)

Appendix B: Error estimation of relative free-energy in TDSMC

In principle, each sampled configuration $\mathbf{r}^N$ contributes to the Monte-Carlo averages at every thermodynamic state (T,ρ); in practice, such contributions will be substantial only for a more limited range of states, of course. But the fact that each configuration contributes to more than one state means that the estimates of the averages that must be combined to obtain the relative free energy (cf. equation (7)), namely

$$B(T_i, \rho_i) \equiv \langle \exp(-\beta_i U(\mathbf{r}^N, L_i))/\pi \rangle^{\pi}, \tag{22}$$

need not be independent for all the different states (T,ρ) recorded within a single run. The covariances of such averages need to be taken into account, therefore, in estimating the statistical error of the relative free energies for such states.

This is quite simple when one is considering two states (T_i,ρ_i) and (T_j,ρ_j), say, within a *single* TDSMC run (and therefore for *all* the free energy estimates within an investigation using *only* a single run, as in the OB version of the present study). We then have for the relative reduced excess free energy

$$\frac{\beta_j A_j^{\mathrm{ex}}}{N} - \frac{\beta_i A_i^{\mathrm{ex}}}{N} = S(T_j, \rho_j) - S(T_i, \rho_i) \tag{23}$$

where

$$S(T_i, \rho_i) \equiv \frac{-\log B(T_i, \rho_i)}{N} + (tc)_i$$

and $(tc)_i$ denotes the tail correction. Thus the square of the standard deviation of the estimate is simply

$$v(T_j, \rho_j) + v(T_i, \rho_i) - 2c(T_j, \rho_j; T_i, \rho_i)$$
$$\equiv \Lambda(T_j, \rho_j; T_i, \rho_i) \tag{24}$$

where $v(T_i,\rho_i)$ is the variance of $S(T_i,\rho_i)$ and $c(T_j,\rho_j;T_i,\rho_i)$ is the covariance of $S(T_j,\rho_j)$ and $S(T_i,\rho_i)$. These quantities are easily written in terms of the variances of and the covariance between the averages $B(T_i,\rho_i)$ and $B(T_j,\rho_j)$ (along with their values). As is usual, each TDSMC run was treated as a succession of shorter blocks of configurations, and block averages of the $B(T_i,\rho_i)$ were collected during the run, so the required variances and covariances are easily estimated (paying the usual attention to the adequacy of the block lengths employed).

The situation is more complex if the investigation has been segmented into several TDSMC runs, and the states in question belong to different segments. As example, we examine the case that arises in the 3S version of the present investigation, where the segments represent different density ranges, and adjoining segments overlap at "seams" which cover a range of temperatures at a single density. Of course, when the states i and j of interest lie within a single such segment their excess free energy difference and its uncertainty can still be estimated in the simple way described in the preceding paragraph. When the states lie in different segments, however, we can nevertheless find the required difference and estimate its error by comparing estimates along the seams between adjoining pairs of segments.

Suppose we have TDSMC runs with target ranges $R^{(1)}, R^{(2)}, \ldots R^{(K)}, \ldots$, the first two segments overlapping at the density $\rho_{\text{seam}}^{(1,2)} = \rho_{\max}^{(1)} = \rho_{\min}^{(2)}$, and so on (in an obvious notation). Suppose initially that state i (i.e. (T_i,ρ_i)) lies in $R^{(K)}$ and state j in the *adjoining* segment $R^{(K+1)}$. Consider also some state, S_t say, lying on the seam, at $(T_t, \rho_{\text{seam}}^{(K,K+1)})$. Then the desired quantity can be written

$$\frac{\beta_j A_j^{\text{ex}}}{N} - \frac{\beta_i A_i^{\text{ex}}}{N} \equiv S_j - S_t + S_t - S_i$$
$$= \left[S_j - S\left(T_t, \rho_{\min}^{(K+1)}\right)\right] + \left[S\left(T_t, \rho_{\max}^{(K)}\right) - S_i\right]. \quad (25)$$

The difference in the first bracket can be estimated entirely from data collected in the run for the $R^{(K+1)}$ segment, and is independent of any local reference state that may have been used in collecting that data, and that in the second, from $R^{(K)}$, similarly. The precision of this estimate can be improved, however, if the seam state at the *single* temperature T_t is replaced by the *average* over the states along the seam for *all* the temperatures T_t for which data was collected. Supposing that there are n_t such states, at temperatures T_t, we have

$$\frac{\beta_j A_j^{\text{ex}}}{N} - \frac{\beta_i A_i^{\text{ex}}}{N} =: \left[S_j - \bar{S}_{\min}^{(K+1)}\right] + \left[\bar{S}_{\max}^{(K)} - S_i\right], \quad (26)$$

where

$$\bar{S}_{\min}^{(K+1)} \equiv \frac{1}{n_t}\sum_{t=1}^{n_t} S\left(T_t, \rho_{\min}^{(K+1)}\right), \quad (27)$$

where the states i and j belong to more-widely-separated segments, say K and M ($M > K$), we have

$$\frac{\beta_j A_j^{\text{ex}}}{N} - \frac{\beta_i A_i^{\text{ex}}}{N} = \left[S_j - \bar{S}_{\min}^{(M)}\right] + \sum_{L=K+1}^{L=M-1}\left[\bar{S}_{\max}^{(L)} - \bar{S}_{\min}^{(L)}\right] + \left[\bar{S}_{\max}^{(K)} - S_i\right], \quad (28)$$

and again each bracket may be estimated from the data of a single segment, and is independent of any reference states used (as it must be). (In the three-segment (3S) application reported in this paper, $M-K$ is at most two, so there is at most one "bridging" segment $R^{(L)}$.)

The expected statistical error of such estimates involves the variances of all the S-terms involved in equations (26) and (28), taking account of equation (27), and also all the covariances between them. Since there will be no correlations between the fluctuations of data in separate runs, the statistical error in the resulting overall estimates equation (26) or (28) can be estimated simply by combining the variances of the separate bracket estimates. These could in turn be obtained by calculating block estimates of each bracket quantity and its square for (statistically independent) blocks within each run. Alternatively, each of these variances can be calculated by an appropriate combination of the variances of $S(T,\rho)$ of all the thermodynamic states involved in the bracket, and all the covariances between them. For example for the first bracket of equations (26) or (28), concerning the $R^{(K)}$ segment, the variance $V^{(K)}$ is given by the combination

$$V^{(K)} = v(T_i,\rho_i) + \frac{1}{n_t^2}\sum_{t=1}^{n_t} v\left(T_t, \rho_{\max}^{(K)}\right) - \frac{2}{n_t}\sum_{t=1}^{n_t} c\left(T_i,\rho_i; T_t, \rho_{\max}^{(K)}\right) + \frac{2}{n_t^2}\sum_{t=1}^{n_t-1}\sum_{s=t+1}^{n_t} c\left(T_t, \rho_{\max}^{(K)}; T_s, \rho_{\max}^{(K)}\right) \quad (29)$$

that for the $R^{(M)}$ term follows by symmetry, while for the bridging, $R^{(L)}$, term of equation (28)

$$V^{(L)} = \frac{1}{n_t^2}\sum_{t=1}^{n_t}\left[v\left(T_t, \rho_{\min}^{(L)}\right) + v\left(T_t, \rho_{\max}^{(L)}\right)\right] + \frac{2}{n_t^2}\sum_{t=1}^{n_t-1}\sum_{s=t+1}^{n_t}\left[c\left(T_t, \rho_{\min}^{(L)}; T_s, \rho_{\min}^{(L)}\right) + c\left(T_t, \rho_{\max}^{(L)}; T_s, \rho_{\max}^{(L)}\right)\right] - \frac{2}{n_t^2}\sum_{t=1}^{n_t}\sum_{s=1}^{n_t} c\left(T_t, \rho_{\min}^{(L)}; T_s, \rho_{\max}^{(L)}\right). \quad (30)$$

For the 3S case reported data was collected at $n_t = 17$ temperatures. This means that in the case of the M and K segments of equation (28) there were $n_t + 1 = 18$ variances and $n_t(n_t+1)/2 = 153$ covariances to be included, for the L segment $2n_t = 34$ variances and $n_t(2n_t - 1) = 561$ covariances; of course, many of the covariances are very small. (The variance of a bridging segment term, $V^{(L)}$, need only be calculated once, of course, and if one is calculating the results relative to a fixed reference state, say in $R^{(K)}$, then evidently $V^{(K)}$ also need only be calculated once.) The 3S errors quoted in the text were estimated in this way.

References

[1] G.M. Torrie, J.P. Valleau. Nonphysical Sampling Distributions in Monte Carlo Free-Energy Estimation: Umbrella Sampling. *J. Comp. Phys.*, **23**, 187 (1977).

[2] G.M. Torrie, J.P. Valleau. Monte Carlo study of a phase-separating liquid mixture by umbrella sampling. *J. Chem. Phys.*, **66**, 1402 (1977).

[3] I.S. Graham, J.P. Valleau. A Monte Carlo study of the coexistence region of the restricted primitive model. *J. Chem. Phys.*, **94**, 7894 (1990).

[4] K.C. Ng, J.P. Valleau, G.M. Torrie, G.N. Patey. Liquid-vapour coexistence of dipolar hard spheres. *Mol. Phys.*, **38**, 781 (1993).

[5] J.P. Valleau. Density-Scaling: A New Monte Carlo Technique in Statistical Mechanics. *J. Comp. Phys.*, **96**, 193 (1991).
[6] J.P. Valleau. The Coulombic phase transition: Density-scaling Monte Carlo. *J. Chem. Phys.*, **95**, 584 (1991).
[7] J.P. Valleau. Density-scaling Monte Carlo study of subcritical Lennard-Jonesium. *J. Chem. Phys.*, **99**, 4718 (1993).
[8] B.A. Berg, T. Neuhaus. Multicanonical algorithms for first-order phase transitions. *Phys. Lett.*, **B 267**, 249 (1991).
[9] B.A. Berg. Multicanonical reversions. *J. Stat. Phys.*, **82**, 323 (1995).
[10] G.N. Patey, J.P. Valleau. The free energy of spheres with dipoles: Monte Carlo with multistage sampling. *Chem. Phys. Lett.*, **21**, 297 (1973).
[11] G.M. Torrie, J.P. Valleau. Monte Carlo free energy estimates using non-Boltzmann sampling: Application to the subcritical Lennard-Jones fluid. *Chem. Phys. Lett.*, **28**, 578 (1974).
[12] G.M. Torrie, J.P. Valleau. Monte Carlo study of a phase-separating liquid mixture by umbrella sampling. *J. Chem. Phys.*, **66**, 1402 (1977).
[13] K. Naganishi, S. Okazaki, K. Ihari, T. Higuchi, H. Tanaka. Free energy of mixing, phase stability and local composition in Lennard-Jones liquid mixtures. *J. Chem. Phys.*, **76**, 629 (1982).
[14] D. Frenkel, A.J.C. Ladd. New Monte Carlo method to compute the free energy of arbitrary solids. Application to the fcc and hcp phases of hard spheres. *J. Chem. Phys.*, **81**, 3188 (1984).
[15] D. Frenkel. Stability of the high-pressure body-centered-cubic phase of helium. *Phys. Rev. Lett.*, **56**, 858 (1986).
[16] C.Y. Lee, H.L. Scott. The surface tension of water: A Monte Carlo calculation using an umbrella-sampling algorithm. *J. Chem. Phys.*, **73**, 4591 (1980).
[17] J.P. Valleau. Thermodynamic-scaling methods in Monte Carlo and their application to phase equilibria. In *Monte Carlo Methods in Chemical Physics, Advances in Chemical Physics*, D.M. Ferguson, J.I. Siepmann, D.G. Truhlar (Eds.), Vol. 105, pp. 369–404, Wiley/Interscience, New York (1999).
[18] N.V. Brilliantov, J.P. Valleau. Thermodynamic scaling Monte Carlo study of the liquid-gas transition in the square-well fluid. *J. Chem. Phys.*, **108**, 1115 (1998).
[19] J.P. Valleau. Temperature-and-density-scaling Monte Carlo: Isothermal-isobaric Thermodynamics of Lennard-Jonesium. *Mol. Simul.*, **31**, 255 (2005).
[20] J.P. Valleau. A Thermodynamic-scaling Study of Gibbs-ensemble Monte Carlo. *Mol. Simul.*, **29**, 627 (2003).
[21] J.P. Valleau, paper in preparation.
[22] J.P. Valleau, S.G. Whittington. A guide to Monte Carlo for statistical mechanics: 1 highways. In *Statistical Mechanics. Part A: Equilibrium Techniques*, Bruce Berne (Ed.), p. 137, Plenum, New York (1977).
[23] G.M. Torrie, J.P. Vallean. Monte Carlo study of a phase-separating liquid mixture by umbrella sampling. *J. Chem. Phys.*, **66**, 1402 (1977).
[24] J.J. Nicolas, K.K. Gubbins, W.B. Streett, D.J. Tildesley. Equation of state for the Lennard-Jones Fluid. *Mol. Phys.*, **37**, 1429 (1979).
[25] N.B. Wilding. Critical-point and coexistence-curve properties of the Lennard-Jones fluid: A finite-size scaling study. *Phys. Rev. E*, **52**, 602 (1995).
[26] J.K. Johnson, J.A. Zollweg, K.E. Gubbins. Lennard-Jones equation of state revisited. *Mol. Phys.*, **78**, 591 (1993).
[27] M. Mecke, A. Mueller, J. Winkelmann, J. Vrabec, J. Fischer, R. Span, W. Wagner. An accurate van der Waals type equation of state for the Lennard-Jones fluid. *Int. J. Thermophys.*, **17**, 391 (1996).
[28] See for example L. Fox, D.F. Mayers. *Computing Methods for Scientists and Engineers*, Oxford University Press, Oxford (1968).
[29] J. Kolafa, L. Horst, K. Aim, I. Nezbeda. The Lennard-Jones fluid revisited: Computer simulation results. *Mol. Simul.*, **11**, 305 (1993).
[30] K. Ding, J.P. Valleau. Umbrella-sampling realization of 'Widom' chemical potential simulation. *J. Chem. Phys.*, **98**, 3306 (1993).
[31] A. Lotfi, J. Vrabec, J. Fischer. Vapour liquid equilibria of the Lennard-Jones fluid from the NpT plus test particle method. *Mol. Phys.*, **76**, 1319 (1992).
[32] B. Smit, D. Frenkel. Calculation of the chemical potential in the Gibbs ensemble. *Mol. Phys.*, **68**, 951 (1989).
[33] A.Z. Panagiotopoulos. Direct determination of phase coexistence properties of fluids by Monte Carlo simulation in a new ensemble. *Mol. Phys.*, **61**, 813 (1987).
[34] A.Z. Panagiotopoulos, N. Quirke, M. Stapleton, D.J. Tildesley. Phase equilibria by simulation in the Gibbs ensemble. Alternative derivation, generalization and application to mixture and membrane equilibria. *Mol. Phys.*, **63**, 527 (1988).
[35] D.J. Adams. Calculating the high-temperature vapour line by Monte Carlo. *Mol. Phys.*, **37**, 211 (1979).
[36] J.R. Errington. Direct calculation of liquid-vapour phase equilibria from transition matrix Monte Carlo simulation. *J. Chem. Phys.*, **118**, 9915 (2003).
[37] Y.C. Kim, M.E. Fisher. Aymmetric fluid criticality. II Finite-size scaling for simulations. *Phys. Rev.*, E**68**, 041506 (2003).
[38] N.B. Wilding, A.D. Bruce. Density fluctuations and field mixing in the critical fluid. *J. Phys. Cond. Matter*, **4**, 3087 (1992).
[39] J.P. Valleau, G.M. Torrie. Heat capacity of the restricted primitive model near criticality. *J. Chem. Phys.*, **108**, 5169 (1998).
[40] J.P. Valleau, G.M. Torrie. Further remarks on the heat capacity of the restricted primitive model. *J. Chem. Phys.*, **117**, 3305 (2002).